修士学位論文

Development of MicroMEGAS for 3D position determination of anti-hydrogen annihilation in CUSP trap

カスプトラップ中での反水素消滅に対する MicroMEGAS三次元位置検出器システムの開発

2014年度

広域科学専攻 相関基礎科学系

学籍番号 31-136902

石川 彰一郎

Contents

Chapter 1

Introduction

We have been conducting a research program using antiprotons at CERN (European Organization for Nuclear Research) which is located in the suburbs of Geneva in Switzerland. CERN can mainly supply high energy protons to various experiments of accelerator science using LHC like ATLAS and CMS, etc. They are well-known for their discoveries of the Higgs boson in recent years. On the other hand, the experiments of antimatter science are performed at AD (Antiproton Decelerator) in CERN. AD is unique in its ability to provide low energy antiprotons, and many physics research groups in the world have been working there for the purpose of studying the antimatter science. ASACUSA (Atomic Spectroscopy And Collisions Using Slow Antiprotons) is one of the antimatter research groups, which has been engaged in studies using slow antiprotons, which includes the atomic collision experiment using ultraslow antiprotons, the antiprotonic-helium experiment, the antihydrogen experiment using the CUSP trap and others. We are working as a part of the ASACUSA collaboration with a unique MUSASHI (Monoenergetic Ultra Slow Antiproton Source for High-precision Investigation) apparatus. We have been developing various techniques toward the production and spectroscopy of antihydrogen aiming at the test of CPT symmetry.

1.1 Hydrogen and Antihydrogen

A particle and its antiparticle in theory have the same mass, life time, charge and magnetic moment except their signs. This is derived from the CPT theorem:

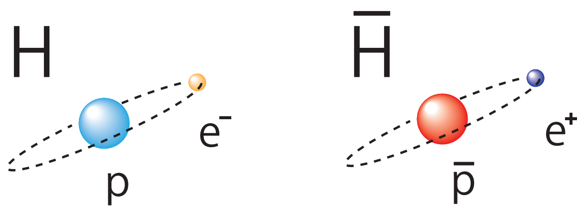

Figure 1.1: A schematic drawing of a hydrogen and an antihydrogen.

when the three conversions of Charge, Parity, Time, are operated to the world at the same time, physical processes of the converted world are completely the same as those of the primary world. Antihydrogen, which consists of antiproton and positron, is a counterpart of hydrogen. It is the simplest antiatom as hydrogen is the simplest atom of all. The antihydrogen is the only antiatom that can be created by experiment. Various physical quantities of hydrogen atom have been measured in high precision. According to the CPT symmetry, they should be the same as those of antihydrogen completely. If any differences between hydrogen and antihydrogen are found, we can raise a question to the authenticity of the fundamentals of the quantum physics. Now we have focused on the hyperfine structure (HFS) of ground-state antihydrogen. That of hydrogen has measured by the maser experiment with high precision[1][2] as

$$\nu_{\mathrm{HFS}} = 1\,420\,405\,751.766\,7(9)\ \mathrm{Hz}. \tag{1.1}$$

The ν_{HFS} of antihydrogen should be the same as that of hydrogen in theory based on CPT symmetry. We aim to test CPT symmetry from a comparison of hydrogen and antihydrogen in terms of the hyperfine structure of their ground states.

Figure 1.2(a) shows a conceptual diagram of hyperfine structure splitting in B = 0. The energy level of ground state is split into two. Furthermore, Figure 1.2(b) shows a conceptual diagram of Zeeman splitting. Under a magnetic field environment, the energy level of the ground-state are split into four. Two of them are called Low field seekers. They move toward an area of lower magnetic field. The other two are called High field seekers, which move toward an area of higher magnetic field.

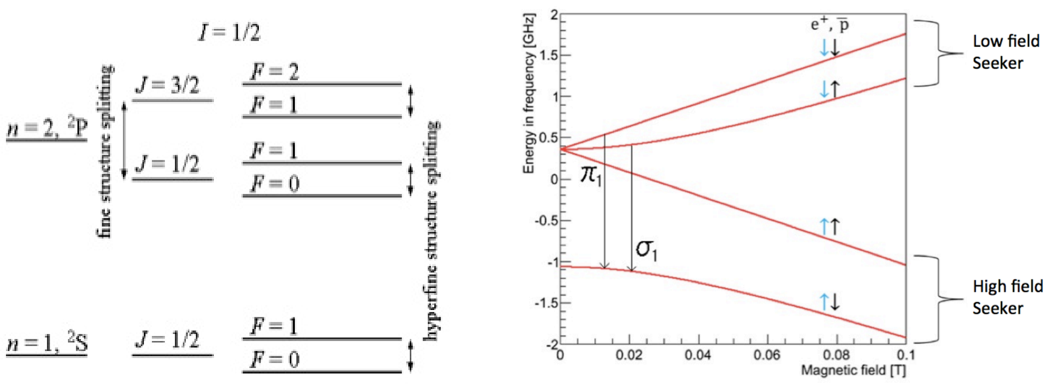

(a) (b)

Figure 1.2: A conceptual diagram of (a)GS-HFS (ground state hyperfine structure) and (b)Zeeman structure in magnetic field.

1.2 Antihydrogen experiment using CUSP trap

A schematic view of the experiment is shown in Figure 1.3.

1.2.1 Setup and procedure

PS, AD and RFQD

Protons accelerated to 26 GeV/c are extracted from Proton Synchrotron and irradiated on an Ir target placed at the entrance of the AD. Then antiprotons are created by pair creation ($\mathrm{p} + \mathrm{p} \rightarrow \mathrm{p} + \mathrm{p} + \mathrm{p} + \bar{\mathrm{p}}$). They are collected by a magnetic horn and injected into AD to be decelerated from 2.6 GeV to 5.3 MeV and cooled by using stochastic cooling and electron cooling technique. For further deceleration, a Radio Frequency Quadrupole Decelerator (RFQD) is placed. The RFQD decelerated the antiprotons down to 120 keV. Thus slow antiprotons are injected into the MUSASHI trap through degrader foils.

MUSASHI trap

MUSASHI trap is located after RFQD to capture the antiprotons. MUSASHI consists of two components: a superconducting solenoid to generate a strong magnetic field along the beam-axis and the Multi-Ring Electrodes (MRE) to make a harmonic electrostatic potential. The setup allows to form the Penning-Malmberg type trap[3] and thus trap charged particles stably. We adopt the electron cooling technique to cool down trapped antiprotons. Prior to the injection of antiprotons, electrons are stored in the trap. Because of the strong magnetic field and their small mass, the electrons quickly lose their energy by synchrotron radiation. When antiprotons are stored in the trap, their energy loss rate due to synchrotron radiation is negligible because of their heavy mass. But they lose their energy by Coulomb scattering with electrons, and heated electrons are cooled by synchrotron radiation. This electron cooling process brings antiprotons's energy down to several eV.

Positron accumulator

Positrons are produced by radioactive decay (β^+ decay) of a ^{22}Na source. They are extracted to the positron accumulator which also consists of both a combination of a superconducting solenoid and a MRE. They lose their energy by N_2 buffer gas cooling and synchrotron radiation. At last they are captured in the extremum of the harmonic potential.

CUSP trap

CUSP trap consists of two components: a superconducting anti-helmholtz coil to make a cusp-formed non-uniform magnetic field and a MRE to make a nested-well potential configuration (see in Fig1.4). In order to produce antihydrogen atoms, at first positrons are transported from the e^+ accumulator and trapped in the CUSP by an harmonic potential. Prior to the antiproton transportation from the MUSASHI, the potential is formed into the nested-well potential. Transported antiprotons lose their energy by interactions with the positrons. Although the positrons are heated up through the interactions, they quickly lose their energy by synchrotron radiation. Both particles are after all cooled down. When a velocity of the positron matches an atomic orbital velocity, the antiproton can capture the positron. Then antihydrogen atom is produced.

As mentioned before, if the energy level of produced antihydrogen is a ground-state, the level is split into LFS or HFS. When produced antihydrogen atoms are low field seekers, they are extracted downstream of the CUSP by the magnetic field.

Hyperfine spectrometer line

In order to perform a ground-state hyperfine spectroscopy, a microwave cavity, a sextupole magnet and a antihydrogen detector are installed downstream of the CUSP trap. The Antihydrogen LFS beam is focused by the sextupole magnet so that they can be detected on the $\bar{\mathrm{H}}$ detector. However if the frequency generated by the microwave cavity matches with the ground-state hyperfine frequency, the direction of magnetic moment of antihydrogen atom flips upside down and LFS state is transformed into HFS state at the cavity. The HFS beam is diverged by the sextupole magnet, therefore the counts of the antihydrogen detector decrease. We can obtain an estimated value of hyperfine frequency by seeking the precise value of the microwave frequency at which the counts of the antihydrogen detector is at the minimum. We will seek for two transition frequencies: π_1 and σ_1 shown in Figure **??**. From equation (1.2) the hyperfine frequency in B = 0 T field can be calculated[4].

$$\sigma_1 - \frac{2(\pi_1 - \sigma_1)^2}{\sigma_1} \tag{1.2}$$

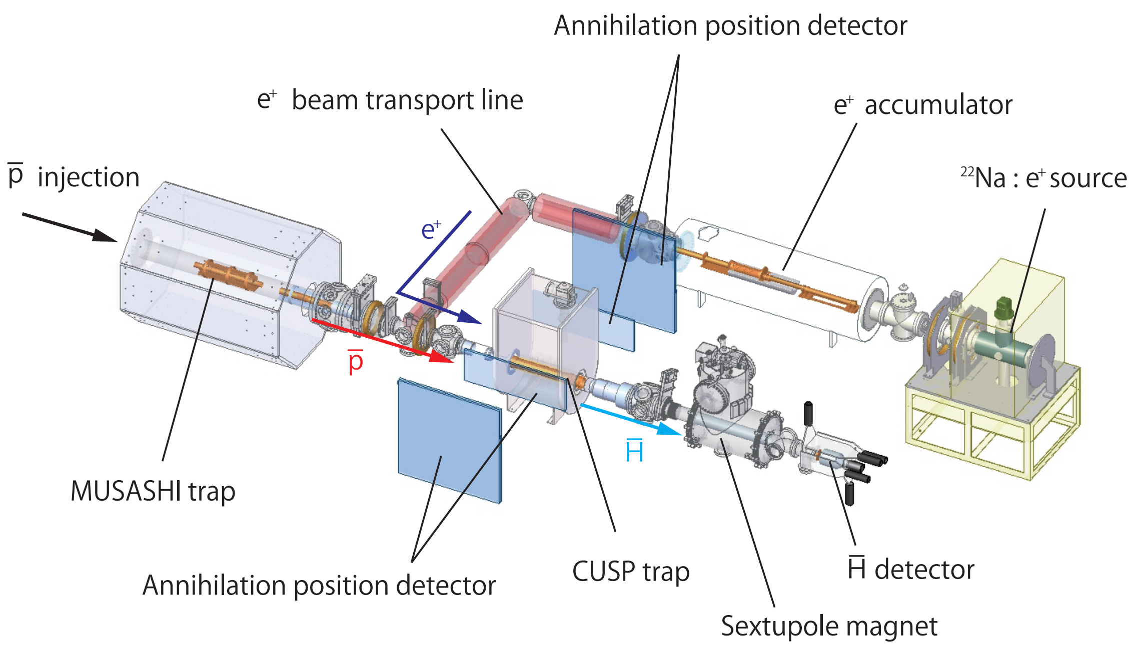

Figure 1.3: Experimental setup of ASACUSA-MUSASHI CUSP experiment (The cavity is not shown in this figure).

1.2.2 Result of the antihydrogen experiment

We have succeeded in producing and detecting antihydrogen atoms in the CUSP trap by using Field Ionization Method[5][6]. An electric potential curve used in this method is shown in the Figure 1.4. There is a so-called nested well potential. Positrons were trapped in the center of the well, which antiprotons are spread over the nested well region. Once antihydrogen atoms are produced in the mixing, they fly out from the potential because they are neutral. Then a part of them can reach the field-ionization well (FIW) at the downstream side. Due to the strong electric field of the FIW, some of the high Rydberg state atoms reaching the FIW can be re-ionized. Their antiprotons are captured at the FIW and accumulated.
We have employed an annihilation position detector which has been developed in Brescia university. It consists of 4 XY-modules, each made of plastic scintillation bars which are 96 cm long, with a rectangular section of 1.5×1.9 cm^2. 2 modules are placed on each side of the CUSP trap, as shown in Figure 1.3. The detector vertex resolution for Z coordinate is around 5-6 cm, and for X-Y it is possibly equal or larger than the size of the MRE[7]. By using this detector, the number of accumulated antiprotons in the FIW can be counted. Furthermore, with an assumption of isotropic angular distribution of produced antihydrogen atoms, the total number of those antihydrogen atoms at the nested well can be estimated. In the previous experiment, we estimated that antihydrogen atoms of 7×10^3 were produced in the mixing with antiprotons of 3×10^5 and positrons of 3×10^6 [5].

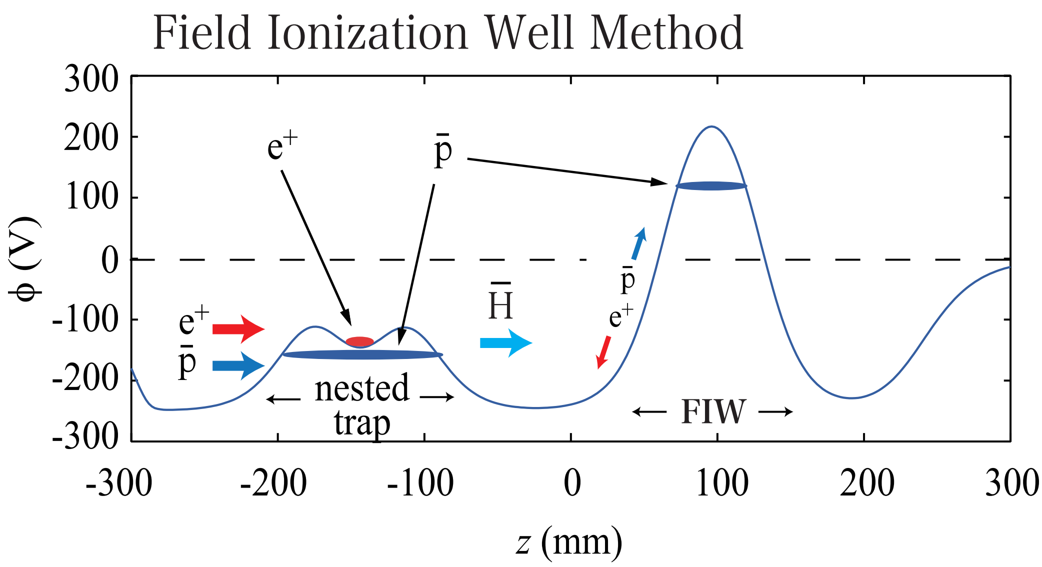

Figure 1.4: Distributions of a nested-well potential configuration and a FIW potential.[5].

At the same time, antiproton annihilation distribution at the nested well is also measured by the annihilation position detector, which is shown in Figure 1.5. Annihilations were observed until 120 s after antiproton injection. In the first 60 s, the peak of reconstructed distribution corresponded to the center of the nested well in which the antiprotons should be trapped. However, in the last 60 s, the peak was divided into two, they seemed to correspond the positions of the local maximum point of the nested well. This would indicate that antiprotons lost their energy because of some interactions with positrons and stayed only at the local maximum. Then they were annihilated by the collision with the residual gases. We should find out the reaction of mixing process in detail toward an effective antihydrogen formation.

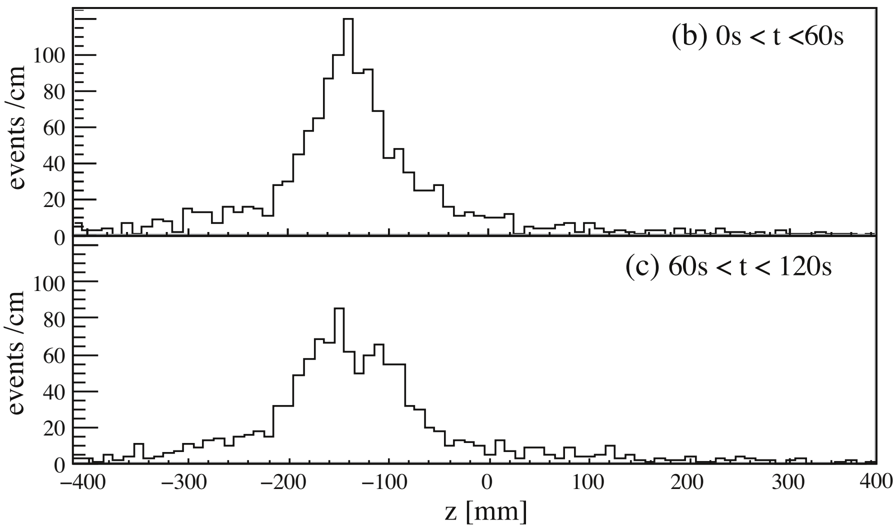

Figure 1.5: A distribution of annihilation signals mixing for 120 s[8]. The data was taken by an annihilation position detector.

1.2.3 Requirement of a new annihilation position detector

As described in the prior subsection, we have the annihilation position detector. But its vertex resolution is not so high. Thus we actually do not know whether the annihilation happens in the center of MRE or on the wall of MRE. Moreover, although an assumption of isotropic angular distribution of produced antihydrogen atoms was taken into account to estimate the number of antihydrogen atoms in the FIW method, we are not sure if this assumption is true or not.

In order to make a further study, we developed a new annihilation position detector which has a higher resolution of vertex reconstruction. Because of its achievable high resolution and spacial limitation of the place where the detector should be mounted, cylindrically-shaped MicroMEGAS detector has been adopted as a new annihilation position detector. According to a vertex simulation, its resolution can reach 1 cm for both r and z directions so that it will be able to identify two kinds of annihilation: one at the center of MRE with residual gases; another on the MRE wall after antihydrogen atoms are produced.

Figure 1.6 shows a procedure of vertex reconstruction by the new annihilation position detector.

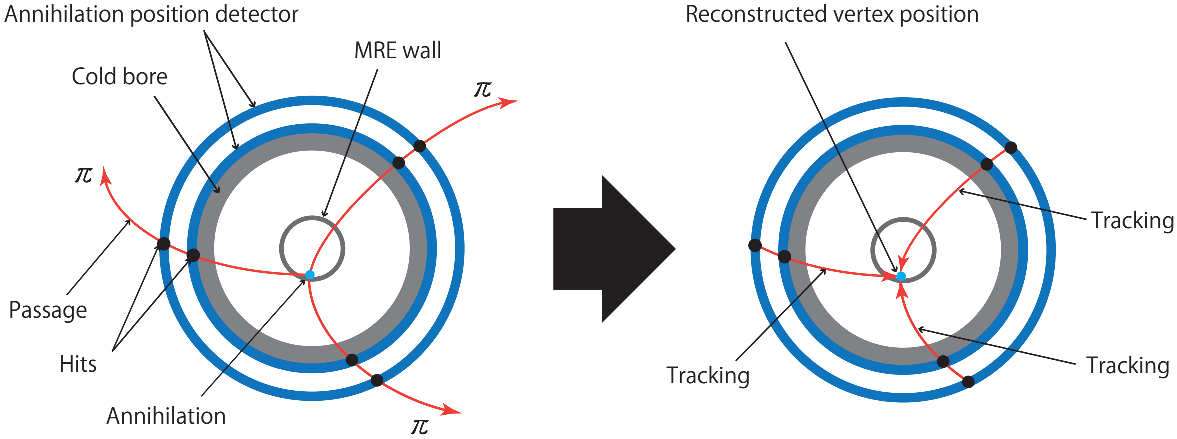

Figure 1.6: A schematic drawing of avertex reconstruction with a new annihilation position detector. Several pions are released from antiproton annihilations. Two pion tracking detectors detect passages of the pions. The passages are fitted by using a tracking algorithm. Then a vertex position which should correspond to the annihilation position is obtained by reconstructing.

Chapter 2

Theory of the passage of particles through matter

2.1 Bethe-Bloch formula

Flying charged particles such as proton, pion and muon are interacted with electrons in matter by Coulomb force. These particles scatter atomic electrons in matter and lose their energy. A part of this energy is converted into the kinetic energy of the atoms in matter while another part of this energy can ionize and excite those atoms. This energy loss per unit length is called stopping power, which can be described as the Bethe-Bloch formula[9],

$$-\frac{dE}{dx} = 2\pi N_A r_e^2 m_e c^2 \rho \frac{Z}{a} \frac{z^2}{\beta^2} \left[\ln \left(\frac{2 m_e \gamma^2 v^2 W_{max}}{I^2} \right) - 2\beta^2 - \delta - 2\frac{C}{Z} \right], \tag{2.1}$$

where r_e and m_e are the classical electron radius and mass, N_A is the Avogadro's number, Z and A are the atomic number and mass number, ρ is the density of absorbing material, I is the mean excitation potential, W_{max} is the maximum energy transfer in a single collision. δ and C are the density and the shell corrections which depend on the particle energies.

Figure 2.1 shows the energy loss of a flying charged particle calculated from the Bethe-Bloch formula. According to this figure, the energy loss reaches minimum at $\beta\gamma \sim 3$ for muon and pion in every material. Particle with such energies is known as a minimum ionizing particle (MIP).

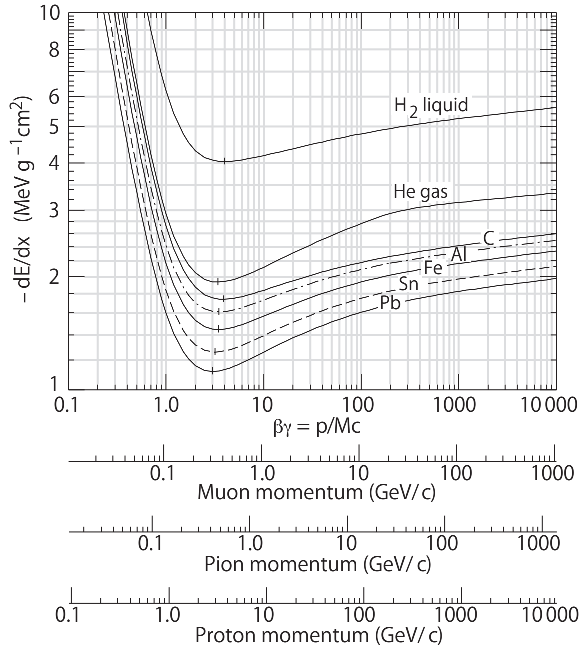

Figure 2.1: An energy loss of a flying charged particle in various materials calculated from the Bethe-Bloch formula[10].

2.2 Gas ionization by charged particles

The excitation and the ionization are the relevant interaction processes for minimum ionizing particles in MicroMEGAS. A charged particle itself ionizes the detector gas in the primary ionization. Some of the ejected electrons have sufficient energy to further ionize the gas in the secondary ionization. In general, the total number of electron-ion pairs can be calculated by

$$N_T = \frac{\mathit{\Delta} E}{W_I}, \tag{2.2}$$

where N_T is the total number of electron-ion pairs, $\mathit{\Delta} E$ is the energy loss per unit length, W_I is the average energy per ion pair.

For the mixture gas, consisting of two gases i and j with a particle number fraction of a and $1-a$, respectively, the total number of electron-ion pairs can be calculated by

$$N_T = N_{T,i} \cdot a + N_{T,j} \cdot (1-a) = \frac{\Delta E}{W_{I,i}} \cdot a + \frac{\Delta E}{W_{I,j}} \cdot (1-a). \tag{2.3}$$

Table 2.1 shows the properties of various relevant gases for gaseous detector. From this list, by calculating the total number of produced electrons, detectable charges on the strips after amplification with gain of $\sim 10^5$(nominal value for gaseous detectors) can be estimated. For example, the total number of electrons produced in the mixture of Ar:iC_4H_{10}=90:10 in 3 mm is given by the equation (2.3) and the Table 2.1 as

$$N_T = (97 \times 0.9 + 220 \times 0.1) \times \frac{3}{10} = 32.8. \tag{2.4}$$

Therefore for the minimum ionization particle, detectable amplified charges, Q, is expressed with the total number of electron-ion pairs, N_T, the amplification gain, G, and the elementary charge, e, which is calculated as

$$Q = N_T \cdot G \cdot e \tag{2.5}$$
$$= 32.8 \times 10^5 \times 1.6 \cdot 10^{-19} \sim 500 \text{ fC}. \tag{2.6}$$

Gas	Density, mg cm^{-3}	E_X eV	E_I eV	W_I eV	$dE/dx\|_{min}$ keV cm^{-1}	N_P cm^{-1}	N_T cm^{-1}
He	0.179	9.8	24.6	41.3	0.32	3.5	8
Ar	1.66	11.6	15.7	26	2.53	25	97
iC_4H_{10}	2.49	6.5	10.6	26	5.67	90	220
CO_2	1.84	7.0	13.8	34	3.35	35	100

Table 2.1: Properties of gases at NTP(20 °C, 1 atom)[11]. E_X, E_I: first excitation, ionization energy; W_I: average energy per ion pair; $dE/dx|_{min}$, N_P, N_T: differential energy loss, primary and total number of electron-ion pairs per cm, for unit charge minimum ionizing particles.

2.3 Muon in cosmic rays

The cosmic rays which can be observed at ground level mainly consist of muons. The proportion of the number of muons in the cosmic rays at ground level is more than 80%. Thus most of the cosmic-ray-derived backgrounds for a particle tracking detector are muon particles. These muon-abundant cosmic rays are originated from so-called primary cosmic rays produced in far-distant supernova explosions which mainly consist of protons rather than muons. When the primary cosmic rays come into the earth, they collide with nitrogen or oxygen molecules int the earth's atmospheres, then charged pions are created by nuclear interaction. Since created charged pions decay rapidly because of their short lifetime, muons, which have relatively long lifetime, are produced at an altitude of 15 km and can reach the ground.

The observed muons at the sea level has a mean energy around 4 GeV and a flat energy distribution below 1 GeV. At sea level, the integral intensity of vertical muons above 1 GeV/c is about 70 $\mathrm{m}^{-2}\mathrm{s}^{-1}\mathrm{sr}^{-1}$[12], which is well-known as the number of 1 $\mathrm{cm}^{-2}\mathrm{min}^{-1}$ for horizontal plane. Also the dependence of the angular distribution for incident muons is in proportion of $\cos^2\theta$, where θ is the zenith angle. This means that the number of muons decreases with their increasing incident angle.

Chapter 3

Principle of MicroMEGAS detector

MicroMEGAS (Micro-MEsh GASeous) detector has contributed in various experiments, since suggested by Y. Giomataris and colleagues in 1996[13]. In recent years, a technology of so-called bulk MicroMEGAS enabled to make a large-area MicroMEGAS for a massive experiment like ATLAS. A new technology to make cylindrical shaped MicroMEGAS is employed for MicroMEGAS at ASACUSA.

In this chapter, the principle of MicroMEGAS detector is described. In section 2.1, the operating principle MicroMEGAS detector is described with a schematic drawing. In section 2.2, we explain about general gases used for MicroMEGAS detector.

3.1 Operating principle of MicroMEGAS

Figure 3.1 is a schematic drawing of the principle of MicroMEGAS detector. MicroMEGAS is a kind of micro pattern gaseous detector, which consists of numerous micro strips printed on a circuit board. Specific gases should be put into MicroMEGAS so that electrons can be produced via ionization by charged particles passing through the detector. The electrons drift to a MicroMesh, and with a certain transparency they transport into the amplification region, where their signal is amplified by a factor of $\sim 10^4$-10^5. The amplified avalanche creates an electric signal on the strips which can be sampled by the front-end electronics. Owing to many strips with small intervals, single hit resolution of MicroMEGAS is in the order of 200-300 μm at nominal operation and without magnetic field. Therefore we can obtain the information on the position where the particle passes through. Furthermore, locating two MicroMEGAS hits in a certain distance makes it possible to track the passing of the particle.
MicroMEGAS consists of 3 types of electrodes, which are described below.

- Drift cathode
  is a flat electrode. Negative high voltage is applied so that the Drift region, which is between the cathode and the Mesh, is in an electric field. Electrons produced in the Drift region drift towards the MicroMesh

- MicroMesh
  is a transparent mesh electrode, held at a less negative potential, which separates the Drift region from the Amplification region, where electron multiplication happens due to the high electric field. The MicroMesh is made of nickel and manufactured by a method of electroforming.

- Anode strips
  are gold-coated cooper strips.The general thickness a strip is 5 μ m. The pitch of the strips is 840 μ m. These strips are connected to the DREAM electronics read-out and kept at ground potential. Electrons multiplied in Amplification region are detected and processed through the DREAM electronics.

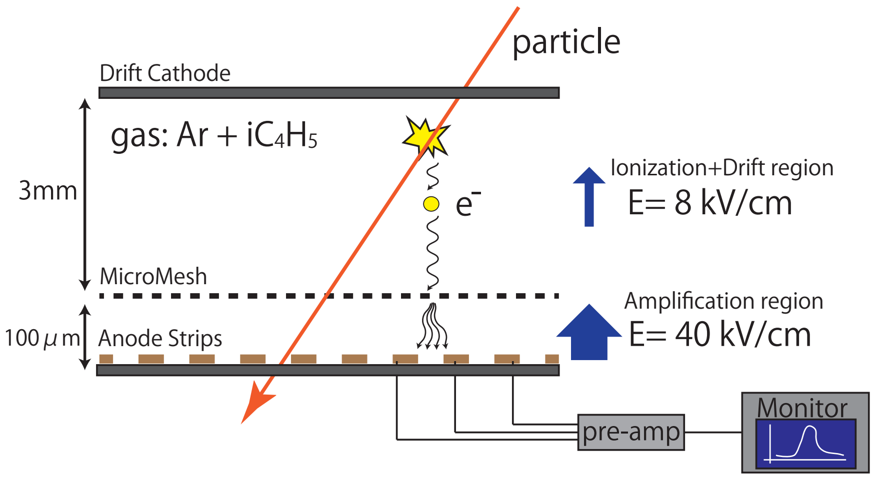

Figure 3.1: A schematic drawing of the principle of the MicroMEGAS.

Figure 3.2 shows a map of the electric field lines around the MicroMesh. In general, electric field in the amplification region is required set to be 5 times higher than that in drift region, otherwise produced primary electrons cannot go through the mesh[14].

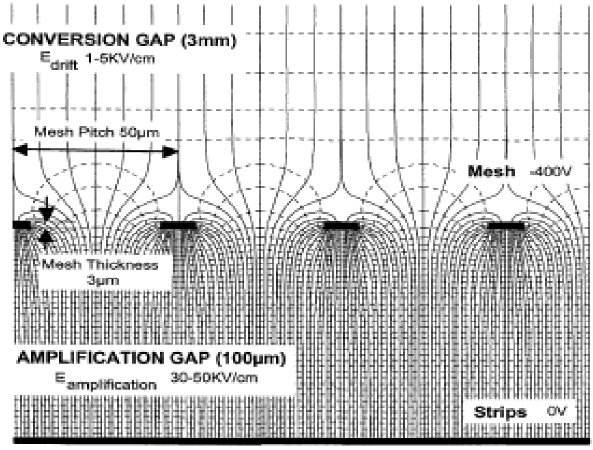

Figure 3.2: A general map of an electric field lines around MicroMesh. (50 μm step, 37 μm diameter of the openings)[14].

3.2 Gases used for MicroMEGAS

The purpose of optimizing the ratio of gas mixture is to provide a good hit resolution of the detector (small avalanche spread at the strips) and high gas amplification (large, detectable signal).
MicroMEGAS is filled with specific mixed gases and they are flowing continuously. These specific gases generally consist of two kinds of gases, one is noble gas and another is polyatomic molecule which is called quencher gas.

- **Noble gas**

  Noble gas accounts for more than 90% of the introduced gas because of its low electron affinity. If produced electrons combine with other gases in Drift region, electrons doesn't come to the anode strips. Therefore, inactive gas is preferred for the gaseous detector.

- **Quencher gas**

  Large number of primary electrons provide larger signal. Also fast drift and low diffusion is needed to achieve good detector hit resolution. Fast ion mobility is needed for quick clearance of positive ions to inhibit space charge effects. This is achieved by polyatomic gas (isobutane, iC_4H_{10}), which provide large number of primaries and helps reducing the number of collisions, and absorbs UV photons emitted by the excited atoms. The UV can produce some unexpected electrons, which leads to a signal diffusion. Several % of polyatomic gas is generally introduced into MicroMEGAS detector to fulfill the role.

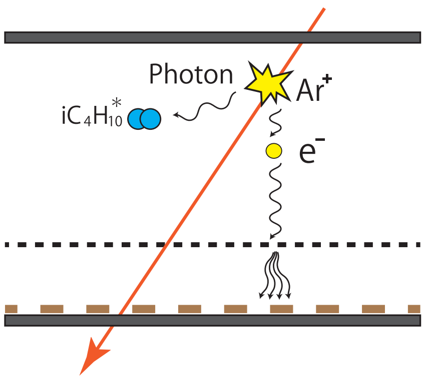

Figure 3.3: A schematic drawing of the role of Ar gas and quencher gases.

Chapter 4

ASACUSA MicroMEGAS Tracker

We have been developing the ASACUSA MicroMEGAS Tracker (AMT) closely collaborating with CEA Saclay MicroMEGAS team. In August 2014, the AMT detector was installed into the antihydrogen experiment successfully. Mainly due to the limited space inside the magnet in which AMT has been installed, several architectural requirements had been considered. Eventually the AMT detector with many remarkable features was produced to meet the requirements. During the production, various brand-new technologies which have never been used before were employed such as;

1. cylindrical shaped detector with two layers
2. 3D printed frames
3. new print pattern of strips
4. smaller than other detectors

Success with these techniques would contribute not only to ASACUSA experiment but also to other various experiments.

In this chapter, all the components of the AMT system are described. In section 4.1, the structure of our MicroMEGAS is described. In section 4.2, the trigger scintillator system is described. In section 4.3, the electronics of the AMT is described. In section 4.4, the gas mixture in use and the gas handling system are described.

During the beamtime in 2014, we had only used an upside part of MicroMEGAS as a half-cylindrical AMT.

4.1 Structure of AMT

4.1.1 Structure

The AMT consists of two cylindrical MicroMEGAS: inner cylinder and outer cylinder. Each cylinder was split into two such as upside half-cylinder and downside half-cylinder. Therefore the AMT consists of four half-cylindrical MicroMEGAS layers: upside inner layer, upside outer layer, downside inner layer and downside outer layer. An assembly drawing and design drawings of the half-cylindrical layers are shown in Figure 4.1, 4.2 and 4.3.

As seen in these drawings, the length along z-axis is roughly 70 cm, of which roughly 40 cm is active area (described in the following subsection). The radius of each inner and outer layer at the planning phase is 78.5 mm and 88.5 mm, respectively. Thus the interval of the layers is 1 cm. Because the AMT had to be mounted in a limited space between a stainless cold bore and a bore of the double CUSP magnet (described in the following subsection), the layers whose interval is only 1 cm had to be manufactured although a general interval of two layers is much larger to obtain a high vertex resolution.

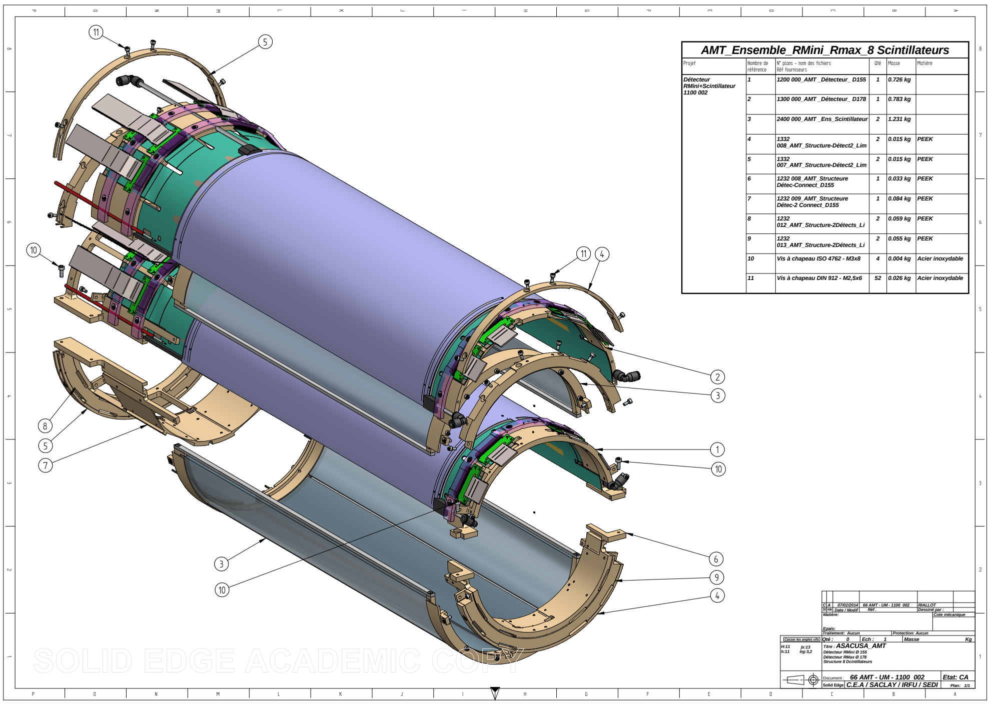

Figure 4.1: Design drawings of AMT detector(1).

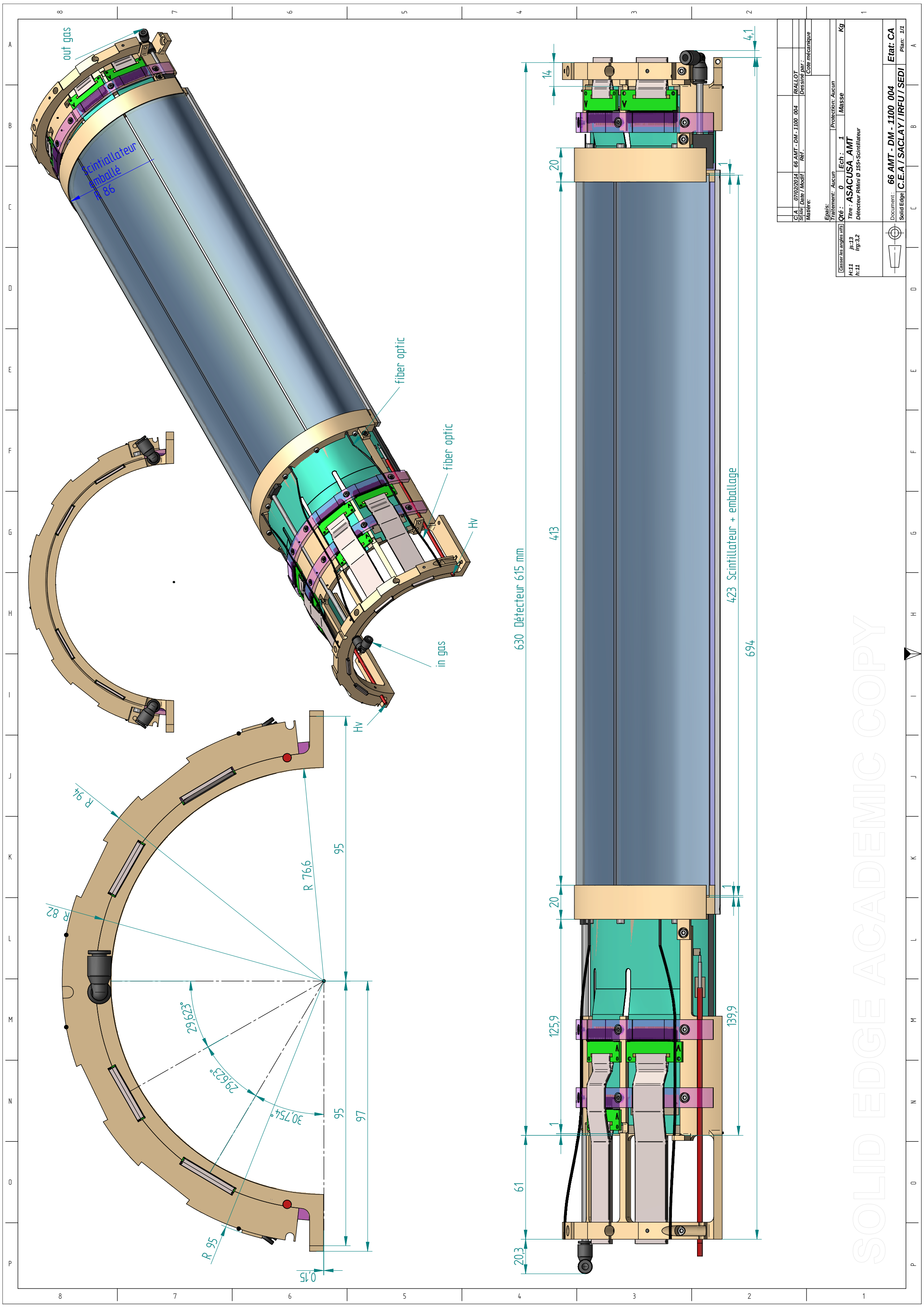

Figure 4.2: Design drawings of AMT detector(2).

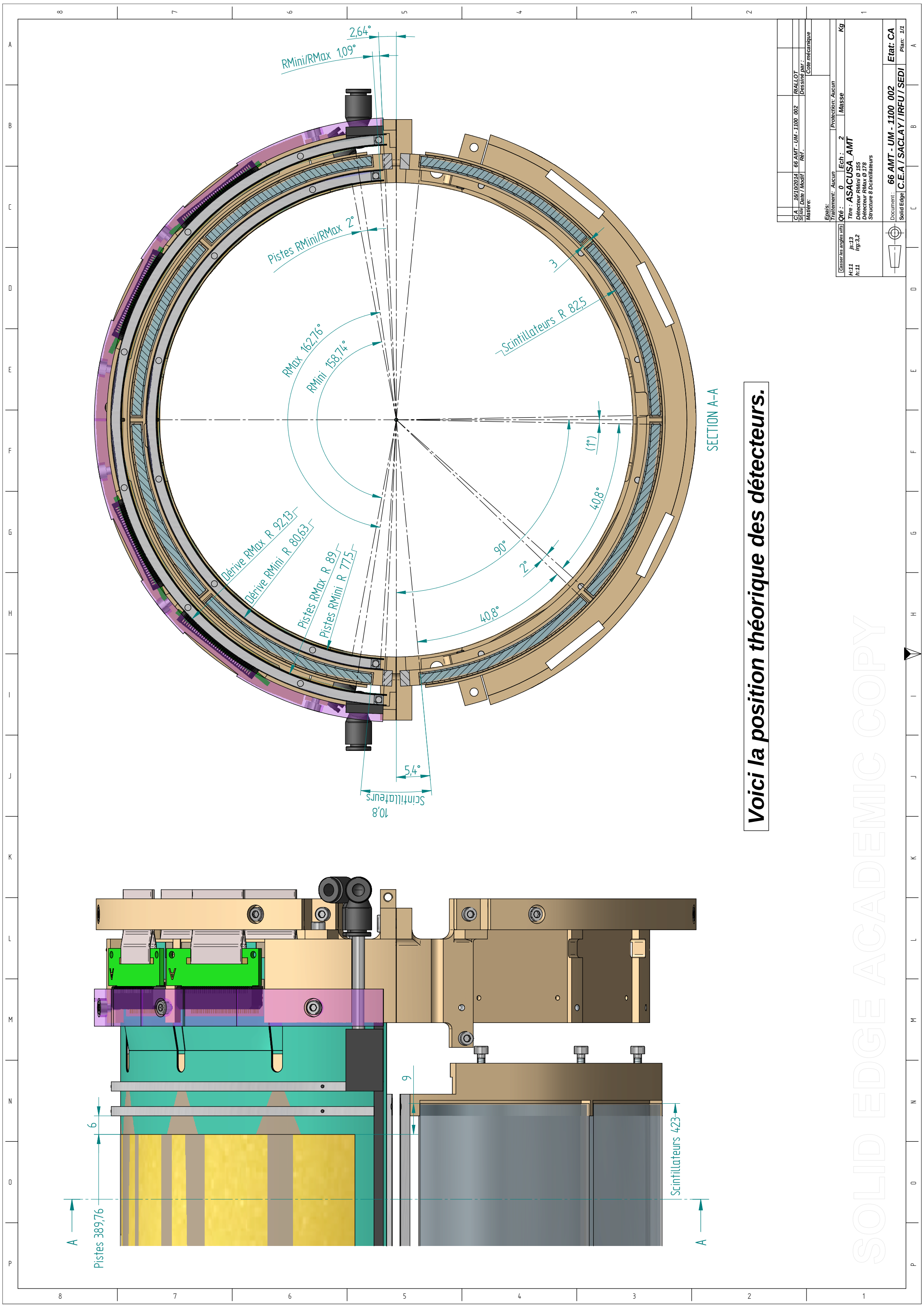

Figure 4.3: Design drawings of AMT detector(3).

After all four layers were assembled, the AMT looked cylindrical-shaped appearance as shown in Figure 4.4. Brown areas shown in both pictures are AMT active areas on which numerous strips are mounted to detect signals. In the picture (b), we can see scintillator bars mounted on the inner layer. The scintillators are covering the active areas of the outer and inner layers. We use the scintillators as a triggering system (described in a following section in detail).

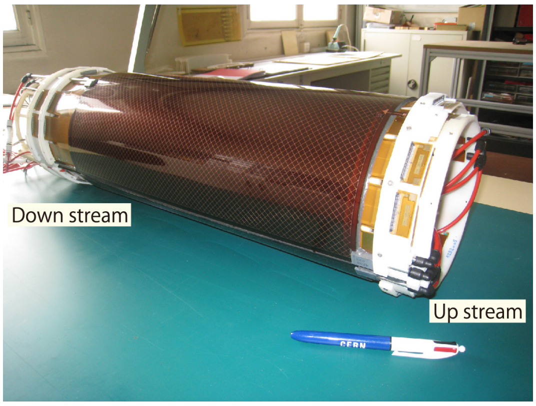

(a) A picture of the cylindrical-shaped AMT after assembling.

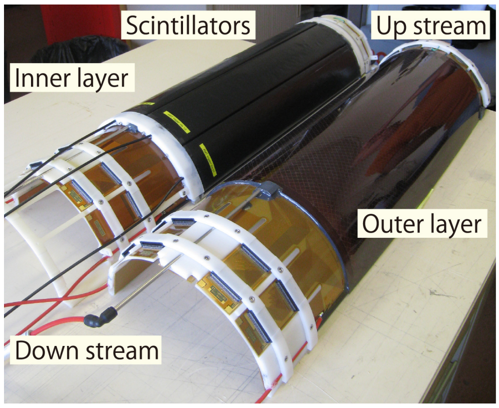

(b) A picture of outer and inner layers with scintillators.

Figure 4.4: Pictures of a cylindrical-shaped AMT detector.

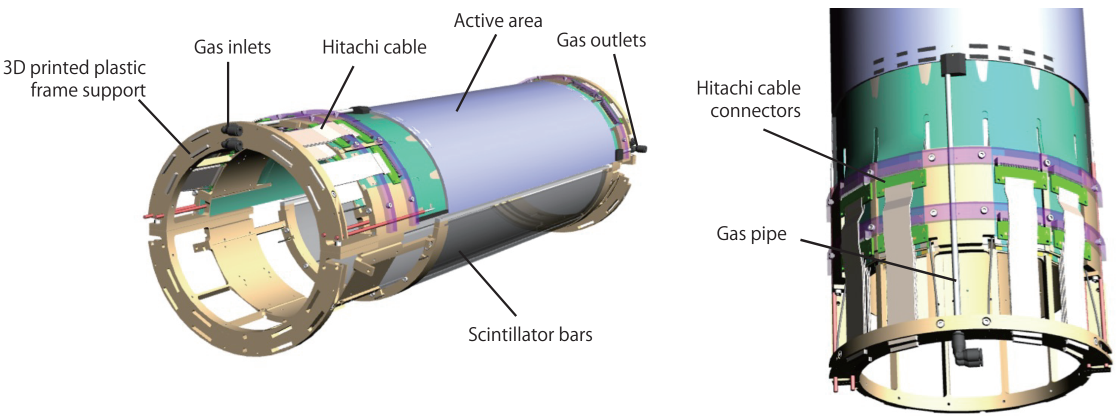

Figure 4.5: CAD illustrations of an AMT detector, which shows many connections.

As seen in Figure 4.5, many connectors and various kinds of cables are connected to upstream and downstream edges; HV cables for mesh and cathode, GND lines, gas tubes of inlet and outlet, optical fibers used for scintillators and multi micro-coaxial cables (Figure 4.6(a)) for readout of strips. Connections of this complex design to other structures is completely fixed by using 3D printed frames (Figure 4.6(b)).

Figure 4.6: (a)A picture of 2m long micro-coaxial cable(Hitachi cable)[15][16]. (b)A picture of 3D printed frame on which Hitachi cables are connected.

Figure 4.7 shows a picture of an experimental setup in 2014. The AMT has installed inside the CUSP magnet. Next to the CUSP magnet, we have prepared a rack on which all handling system of the AMT have been mounted, such as a gas operation, NIM modules, FEU boards, interlock and other electronics.

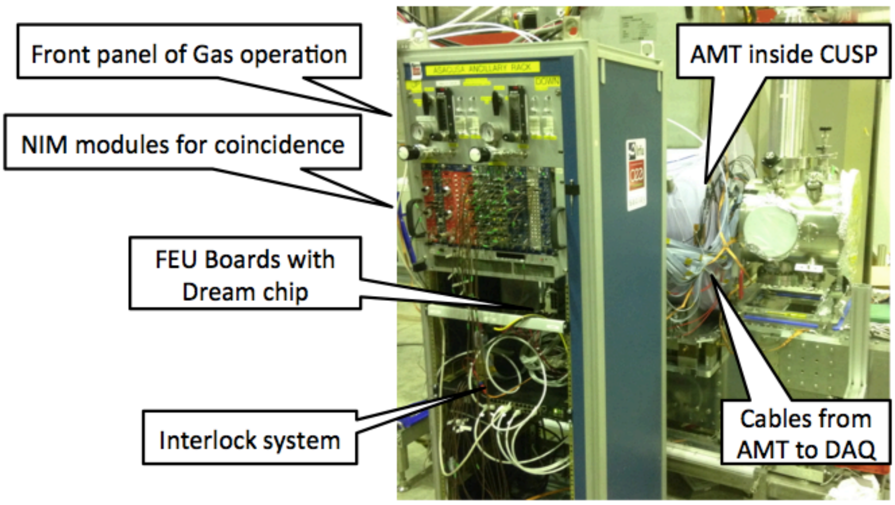

Figure 4.7: A picture of the experimental setup of AMT.

4.1.2 Installation into the Double CUSP magnet

A Double CUSP magnet (we call it "CUSP" in this thesis) was also developed and installed into the experiment before the beamtime in 2014 together with the AMT, which is shown in Figure 4.8(a). The previous CUSP magnet was replaced with it for its improvement of focusing performance of antihydrogen beam and a reduction of the leakage of magnetic field. It has three superconducting coils to which the electric currents of alternately-opposite directions are applied as shown in Figure 4.8(b). By this way, a cusp magnetic field is created in two regions between each neighbor coils. That is, the double CUSP magnet consists of two anti-helmholtz coils, which enables us to obtain doubly-focused antihydrogen beam.

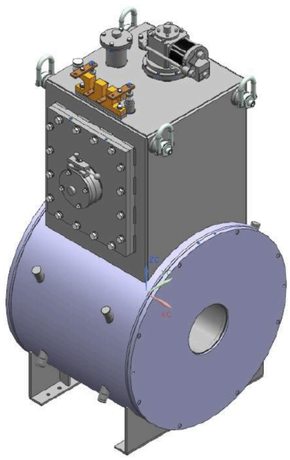

(a)

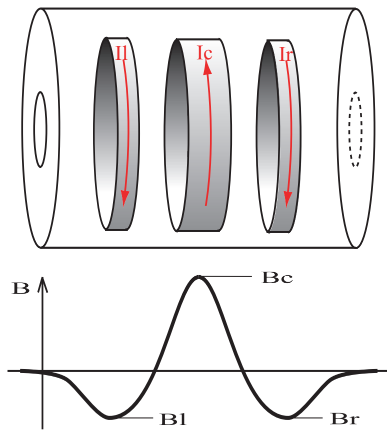

(b)

Figure 4.8: Illustrations of (a)the double CUSP magnet, (b)its superconducting coils and created magnetic field.

The double CUSP coils have been completely covered with its magnetic shield to reduce the leakage of magnetic field outside. The length of the shield is 650 mm. The inner diameter of the shield is 200 mm. The AMT mounted on a cold bore has been installed inside the magnet, that is, the AMT is placed between the chamber and inner side of the magnet structure. Figure 4.9 shows a position relation among the AMT, the double CUSP magnet and its magnetic field. The relation was precisely determined from a calibration measurement, which is described in chapter 6. Each layer of the AMT is influenced by non-uniform magnetic field generated by the CUSP, a part of which is placed in the strong magnetic field. Table 4.1 is a list of parameters of the double CUSP magnet.

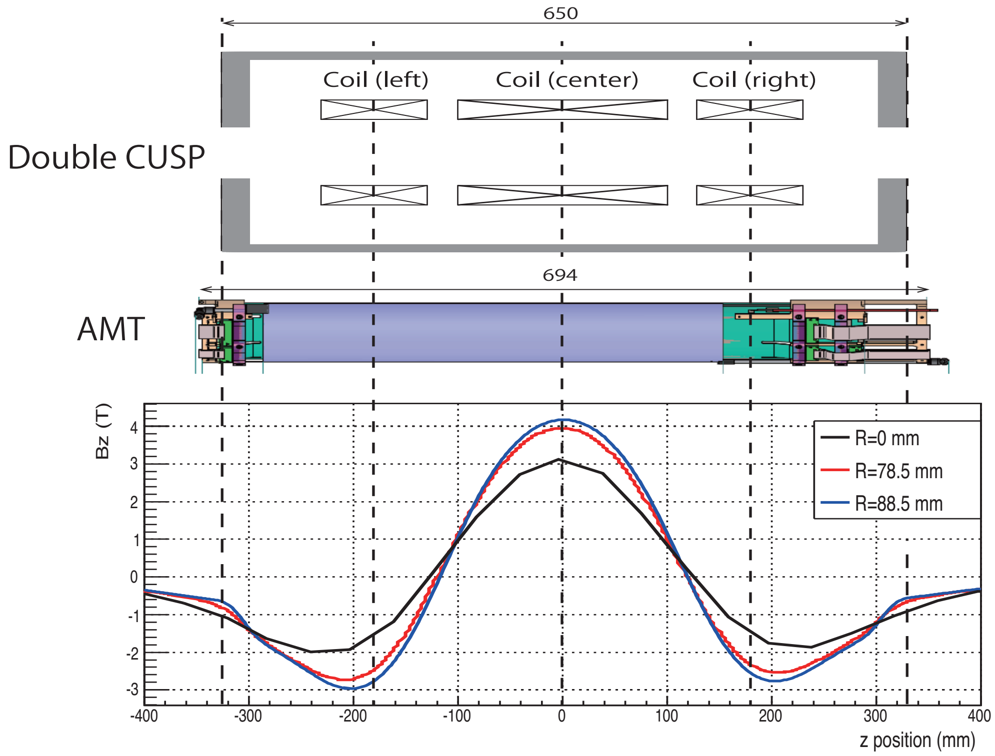

Figure 4.9: An illustration of the position relation among AMT, CUSP magnet and its magnetic field.

Parameter	Coil (left)	Coil (center)	Coil (right)
z position (mm)	-180	0	180
Width (mm)	100	200	100
Inner radius (mm)	135	135	135
Outer radius (mm)	217.1	217.1	217.1
Number of turns (mm)	10143	20384	10143
Material(Superconducting coil)	Nb-Ti, Cu		
Material(Magnetic shield)	SS400, SUS304, SUS316L		

Table 4.1: A list of parameters of Double CUSP magnet[17].

4.1.3 PCB layer

A printed circuit board (PCB) is one of the most important components of MicroMEGAS, which is assembled with cathode electrode and MicroMesh. The region between MicroMesh and PCB layer is in a high electric field. Numerous position-sensitive strips are printed on PCB, the hit position of charged particles can be determined by detecting amplified electrons arriving onto the microstrips. As described in previous section, the cylindrical AMT has four layers of MicroMEGAS: upside inner and outer layers, downside inner and outer layer. So we have four PCB layers as well. In 2014 we had used AMT as half-cylindrical AMT. Thus the AMT has only upside inner and outer PCB layers. Figure 4.10 is a top view of one of the PCB layers in use.

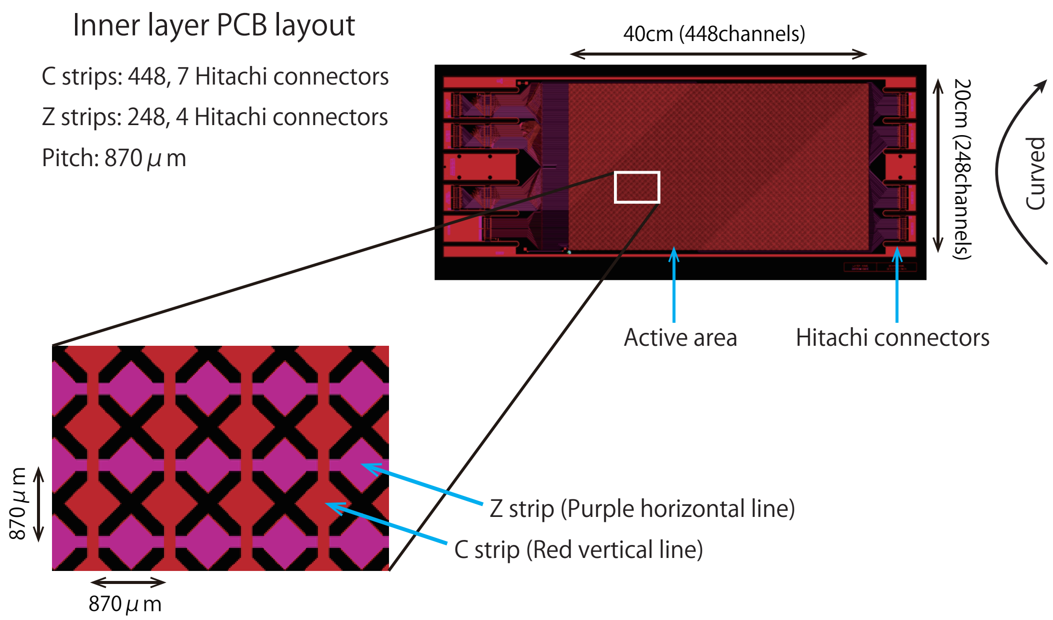

Figure 4.10: Microstrip pattern on the PCB layer.

The printed pattern of strips is an unique layout for AMT, which has never been used before. This layout enables us to determine a hit position two dimensionally with using one PCB layer. This means that strips on horizontal line (Purple line) and strips on vertical line (Red line) are printed perpendicularly on one layer. The horizontal ones are printed on one side of the layer and the others are printed on the other side of the layer. Also small-square pixels are printed throughout one side of the layer, with which strips on both sides are connected electrically. But each strip on both layers are isolated electrically. When the pads receive charges of amplified electrons, induced voltages are read out by the strips in both directions. The horizontal line in Figure 4.10 is a straight line along z-axis so that we call it Z-strip(Z-direction). On inner layer there are 228 Z-strips and on outer layer there are 248 Z-strips. On the other hand, the vertical line in the figure is a curved line along the circumference of the layer so that we call it C-strip(C-direction). There are 448 C-strips on both layer. The pitch size of the strips is 870 μm. The curvatures of outer and inner layer in the basic design phase are $r = 87.5$ mm and $r = 77.5$ mm, respectively.

Hit resolution

The hit resolution is calculated from the pitch size of the strips. As seen in Figure 4.11, charges from a particle on a shaded area are read out by the strip on x_0. The standard divination σ_x is calculated from equation below:

$$\sigma_x^2 = \int_{x_0-\frac{d}{2}}^{x_0+\frac{d}{2}} (x-x_0)^2 P(x) dx, \tag{4.1}$$

where $P(x)$ is the probability when the strip reads outs charges on x. In the case of the uniform distribution, $P(x) = 1/d$. So,

$$\begin{aligned} \sigma_x^2 &= \int_{x_0-\frac{d}{2}}^{x_0+\frac{d}{2}} (x-x_0)^2 \cdot \frac{1}{d} dx && (4.2) \\ &= \frac{1}{d}\left[\frac{1}{3}(x-x_0)^3\right]_{x_0-\frac{d}{2}}^{x_0+\frac{d}{2}} && (4.3) \\ &= \frac{d^2}{12}. && (4.4) \end{aligned}$$

Therefore,

$$\sigma_x = \frac{d}{\sqrt{12}}. \tag{4.5}$$

Since the pitch size of the strips is 870 μm, the theoretical hit resolution becomes 250 μm.

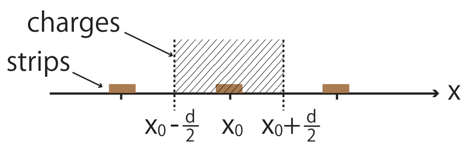

Figure 4.11: A schematic drawing of the resolution of hit. Charges in the shaded area are read out by the strip in the centre.

We have outer and inner layers. In what follows, we call them Rmax and Rmin, respectively. We have Z-strip and C-strip on each layer. Thus there are four projections. For the convenience, we call them RmaxZ, RmaxC, RminZ and RminC, from their combination. Table 4.2 is a list of parameters of the PCB layers. Figure 4.12 is pictures of PCB layers before and after assembly.

Parameter	Outer layer(Rmax)	Inner layer(Rmin)
Number of Z strips	288	248
Number of C strips	448	448
Active area (cm^2)	970	840
Radius (mm)	87.5	77.5
Pitch (μm)	870	
Hit resolution (μm)	250	

Table 4.2: A list of characteristic values of the AMT microstrip structure.

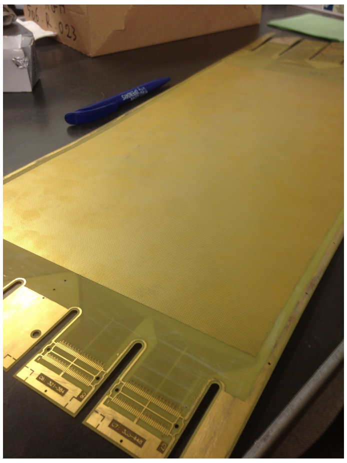

(a) A picture of a raw PCB layer.

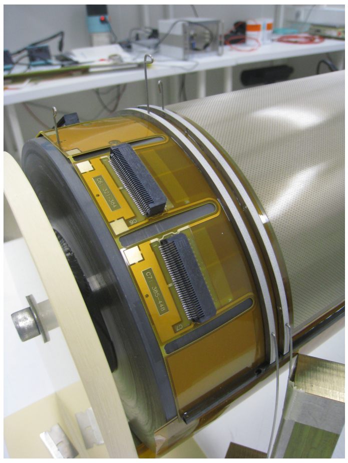

(b) A picture of the PCB after bulking and curving.

Figure 4.12: Pictures of a PCB layer.

4.2 Scintillator and trigger system

4.2.1 Principle of scintillator and PMT

A plastic scintillator is often used on a gaseous tracking detector as a triggering system. It is made of polystyrene-based solvent and adequate amount of anthracene. Advantages of using a plastic scintillator are its fast light emission and its inexpensive price. From this aspect, it is often used for various particle physics.

Molecules and atoms in a scintillator are ionized and excited by a charged particle passing through it. When these excited molecules or atoms are de-excited, scintillation light is emitted equivalent of residual kinetic energy. The wavelength of scintillation light depends on materials of the scintillator, though usually plastic scintillator have a blue light emission. These scintillation light can be detected by the Photo Multiplier Tube (PMT) which is connected to the end of the scintillator. However, PMT also has an unique absorption wavelength. If these emission and absorption wavelengths do not match, some small scintillation signals might be lost and trigger efficiency gets unsatisfactory. To avoid this, it should be taken into account to match these emission and absorption wavelengths. If required, so-called wavelength shift fiber is generally used to match both wavelengths.

Fig 4.13 shows a schematic drawing of the configuration of scintillator, PMT and wavelength shift fiber. Wavelength shift fiber is a thin, long fiber embedded in the surface of the scintillator. The material of the wavelength shift fiber absorbs a scintillation light and re-emits light which has a wavelength that corresponding to the absorption wavelength of PMT. Then the re-emitted lights are detected by the PMT efficiently. Furthermore, there is one more utility of usage of the wavelength shift fiber. It enables to transfer the light for long distance with little transmission loss.

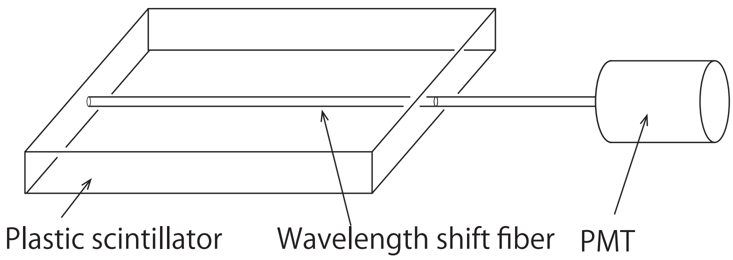

Figure 4.13: A schematic drawing of a principle of a scintillator.

As shown in Fig 4.14, when photocathode in the PMT gets a scintillation light, electrons are emitted by the photoelectric effect. Those electrons are accelerated in the electric field. They collide with the first dynode, which produces secondary electrons. All of them are accelerated again and collide with the second, third dynode, which eventually multiplies electrons by a factor of $\sim 10^5$, then signals are read out.

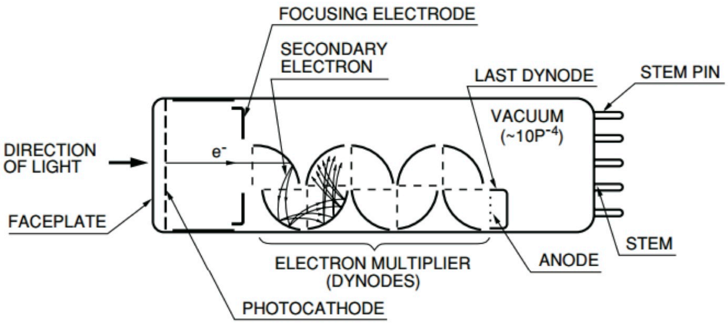

Figure 4.14: A drawing of a principle of PMT[18].

4.2.2 Scintillator bars for trigger system

The role of scintillator for gaseous detector is to provide a trigger signal of particles which pass though the scintillators. Figure 4.15 and 4.16 show a configuration of scintillators of the AMT triggering system. The scintillators are located between inner and outer layer. As seen in the figures, 4 scintillator bars in upper side and

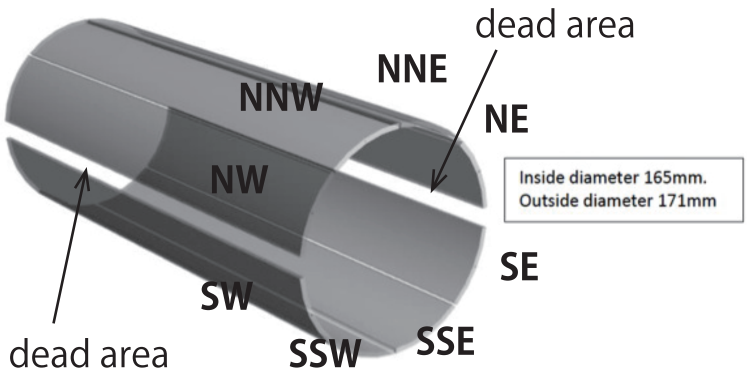

Figure 4.15: A configuration drawing of plastic scintillator segments of AMT.

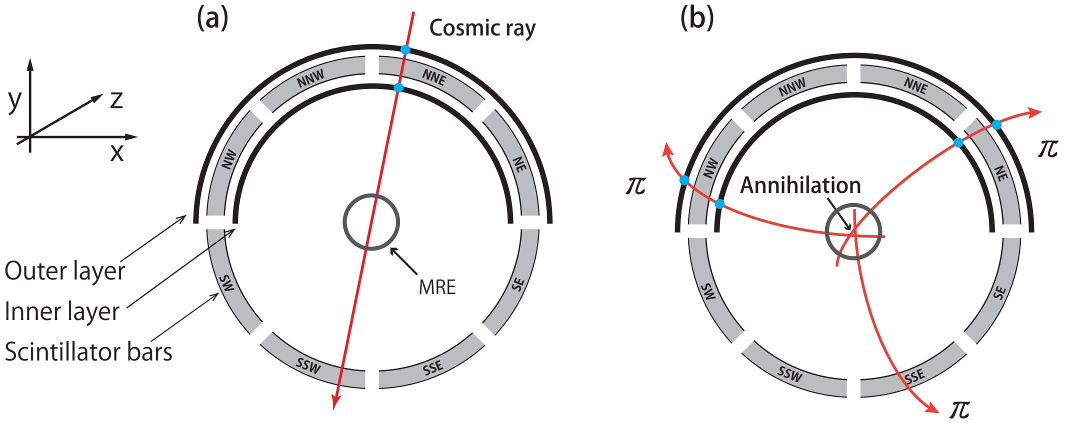

Figure 4.16: A schematic drawing of the configuration of scintillator bars. (a)Passage of cosmic ray. (b)Passage of pions originated form antiproton annihilation.

the other 4 in down side are mounted at the same interval, that are shaped along the circumference. Each of them is named for the compass like NE or SSW from upstream sight. They are completely fixed at the limited space and they have few dead areas, that is, most of the circumference of the cylinder are covered with those 8 scintillator bars. There is only the dead area of 3 cm which is small as compared to the total circumference of 50 cm. As seen in Figure 4.16(a), in principle 2-fold coincidence should be taken as a trigger for the particle comes from outside like cosmic rays. On the other hand, since 2-4 pions, produced by the annihilation of antiproton/anti-hydrogen inside CUSP, should pass the layer at the same time, the condition of more than 2-fold coincidence should be better as a trigger shown in Figure 4.16(b).

Figure 4.17 shows a cross-sectional drawing of a scintillator bar and a wavelength shift fiber. Figure 4.18 shows two pictures of a plastic scintillator bar. The length,

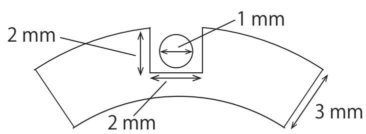

Figure 4.17: A cross-sectional drawing of a scintillator bar and a wavelength shift fiber.

the width and the thickness of a scintillator bar are 42 cm, 7 cm, 3 mm, respectively, and the bar is a bit curved. In addition each scintillator bar has a small groove along the length whose depth and width are 2 mm, respectively. The wavelength shift fiber is glued inside the groove, which diameter is 1 mm. The length of the fiber is 2 m. The other side is connected to an anode of a PMT. The fiber is sheathed with a black material to avoid external light pollution. The scintillator bar on which the fiber has been equipped is wrapped with a material which is coated an reflective foil on scintillator side for an effective light collection and a black sheet on the other side to avoid external light pollution.

The light emitted inside the scintillator is absorbed by the fiber. Then the fiber reemits wavelength-shifted light. The light is guided inside toward the PMT.

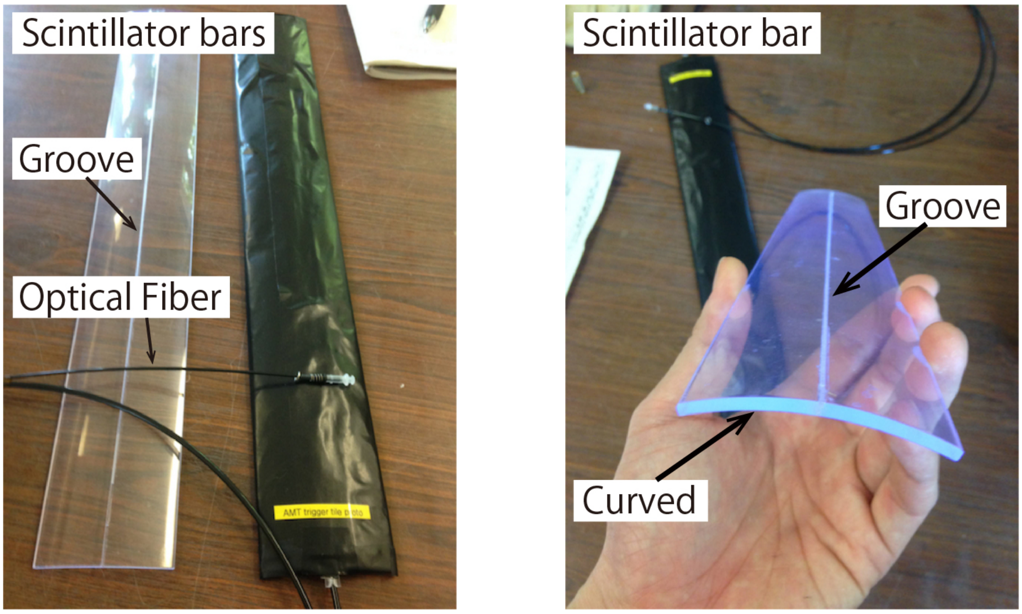

(a) (b)

Figure 4.18: Pictures of scintillator bars used for AMT triggering system. We can see a curved scintillator bar, a groove along the length and an optical fiber.

Figure 4.19 shows a theoretical emission spectra and a measured emission spectra of the scintillator in use[19]. The measured wavelength of maximum emission was 426 nm, which corresponded to the theoretical value. Also the curve of the measured spectra was roughly the same as theoretical one. The various parameters of the scintillator are listed on Table 4.3.

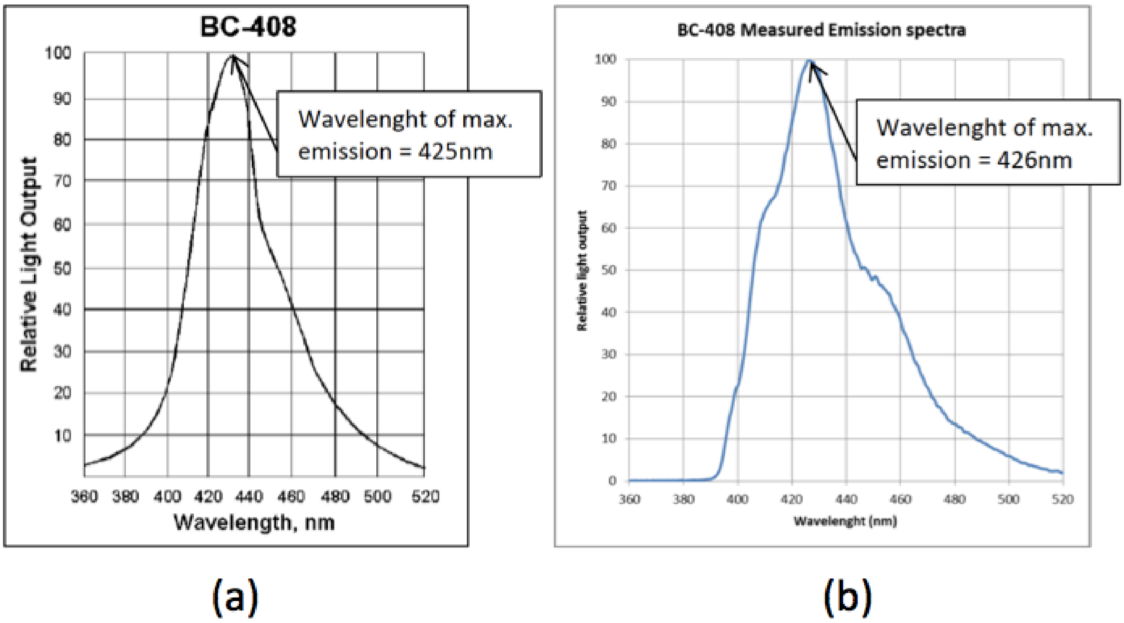

Figure 4.19: Emission spectra of the scintillator in use. (a)A theoretical emission spectra[20] and (b)a measured emission spectra measured in Saclay[19].

Parameter	Value
Base	polyvinyl toluene
Light output, Anthracene	64 %
Rise time	0.9 ns
Decay time	2.1 ns
Light attenuation length (1/e)	210 cm
Wavelength of max emission	425 nm

Table 4.3: A list of the characteristic values of the scintillator in use[20].

Figure 4.20 shows a theoretical and a measured spectra of absorption and emission wavelength of the wavelength shift fiber in use[19]. The measured values of maximum absorption and emission wavelength roughly corresponded to the theoretical values. The fiber change the light wavelength from 425 nm(blue) to 504 nm(green). The various parameters of the wavelength shift fiber are listed on Table 4.4.

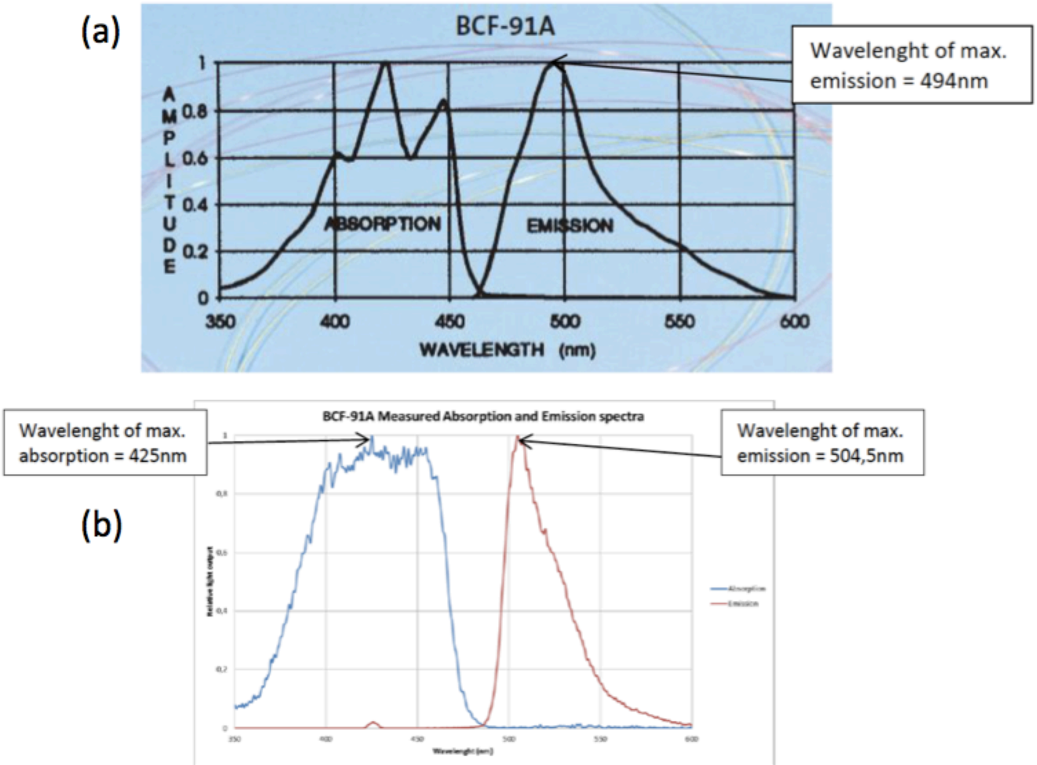

Figure 4.20: Absorption and emission spectra of the wavelength shift fiber in use. (a)A theoretical absorption and emission spectra[21] and (b)a measured absorption and emission spectra measured in Saclay[19].

Parameter	Value
Base	polyvinyl toluene
Light output, Anthracene	64 %
Rise time	0.9 ns
Decay time	2.1 ns
Light attenuation length (1/e)	210 cm
Wavelength of max emission	425 nm

Table 4.4: A list of the characteristic values of the wavelength shift fiber in use[21].

The PMT made by Hamamatsu photonics, model H7546 64-channel multianode type[18], has been adopted. Decreasing the effects of cross-talk, effective 8 channels out of 64 channels whose position has never effected each other has been selected. The characteristic of the PMT is shown in the Table 4.5 and the graphic representation of its gain and quantum efficiency as a function of light wave length are shown in Figure 4.21(a),(b).

Parameter	Value
Spectral response (nm)	300 to 600 (Max 420)
Gain	3×10^5
Cathode effective area (mm^2)	18.1×18.1
Number of dynode stage	12
Quantum efficiency at 390 nm (%)	20
Anode pulse rise time (ns)	1.5
Cross-talk(with 1 mm optical fiber) (%)	2

Table 4.5: A list of the characteristic values of H7546 64ch PMT[18].

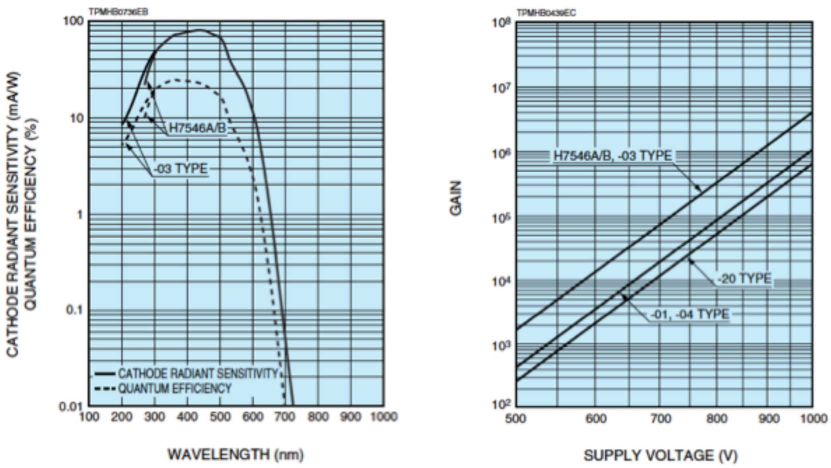

Figure 4.21: Spectra of (a)PMT gain, (b)PMT quantum efficiency of the PMT in use as a function of light wave length[18].

Scintillator efficiency

Figure 4.22 shows a result of an efficiency test in Saclay for each scintillator bars. Measured efficiencies are listed in Table 4.6. By comparison of their efficiencies, we selected efficient 8 scintillator bars out of the 12. Selected ones are labeled.

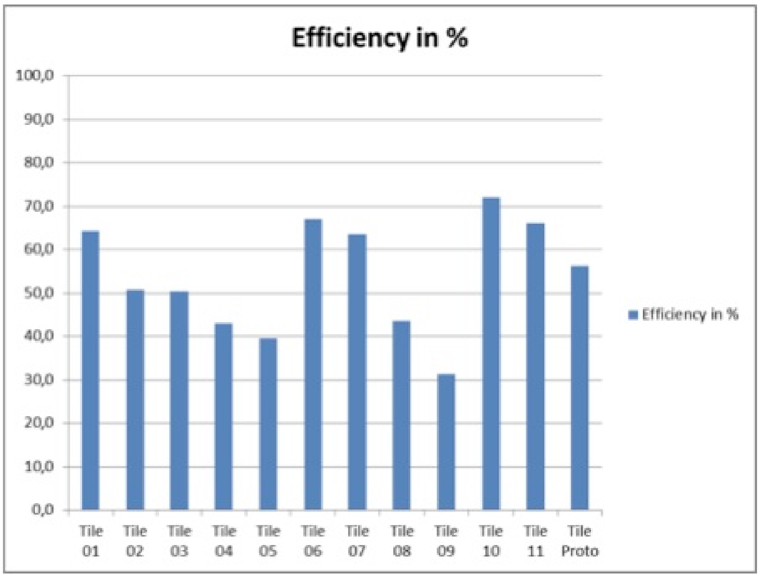

Figure 4.22: A comparison of the scintillator efficiencies[19].

Tile number	Labeled	Efficiency in %	Tile number	Labeled	Efficiency in %
Tile 01	NW	64.3	Tile 07	NE	63.7
Tile 02	SSW	50.7	Tile 08		43.6
Tile 03	SSE	50.4	Tile 09		31.3
Tile 04		43.0	Tile 10	NNE	72.1
Tile 05		39.5	Tile 11	SW	66.2
Tile 06	NNW	67.0	Tile proto	SE	56.3

Table 4.6: A list of the result of the efficiency test[19].

4.2.3 Trigger modules

Figure 4.23 is a picture of trigger NIM modules and HV supply modules mounted on the AMT rack. A block diagram of this system is shown in Figure 4.24. After amplified on the PMT, scintillators signals are processed in the following NIM models. At the first fan-out module, each signal splits into two. One output is fed to the second Amplifier module for trigger logic while another is fed to one of FEUs to be sampled. The signal is amplified at the Amplifier by a factor of 10 and fed to the third Discriminator. Channels which have a signal over threshold can only send "1" with certain time width to the following Coincidence module. In general 2-fold coincidence channel is used, but there are also 1 or 3-fold coincidence channels so far, which is programmable. The final Discriminator is used for tuning output time window. Thus produced coincidence signal is immediately fed to FEU boards as an event trigger.

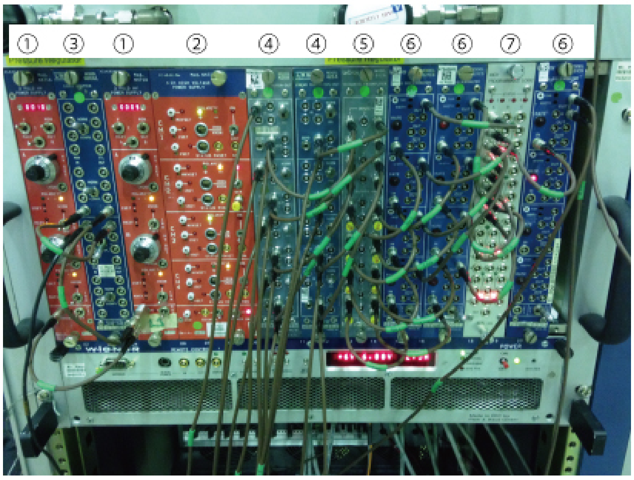

1	HV PS CEAN N471A
2	HV PS CEAN N472
3	Level Adapter LRS 688AL
4	Linear fan-out LSR 428A
5	Amplifier LeCroy 612A
6	Discriminator LeCroy 821CS
7	Coincidence logic N-PL 101

Figure 4.23: A picture of HV power supply modules and Trigger NIM modules.

Figure 4.25 shows a block diagram of the LV and HV power supplies and their interlock system. The interlock system is required to stop HV automatically to protect DREAM chips and FEU electronics against some unexpected sparks in the layers of MicroMEGAS. The HV modules have own inhibit (INH) contact, which is connected to the LV power supply. When sparks happen, that signal is fed to the LV power supply quickly. Then, LV supply commands INH of HV supply to stop applying voltage.

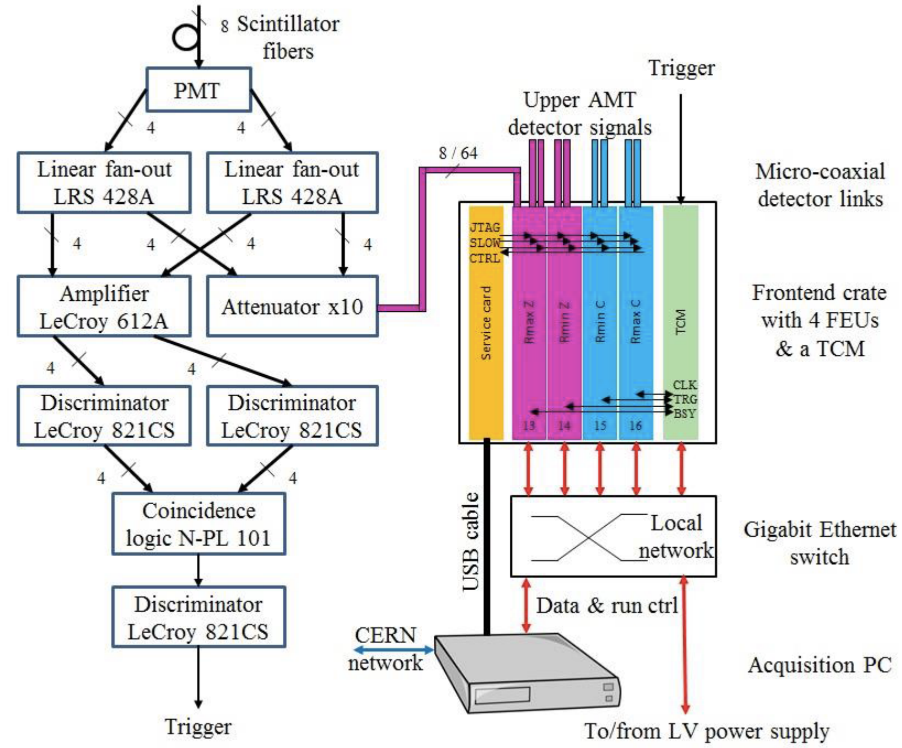

Figure 4.24: A block diagram of trigger and readout system[22].

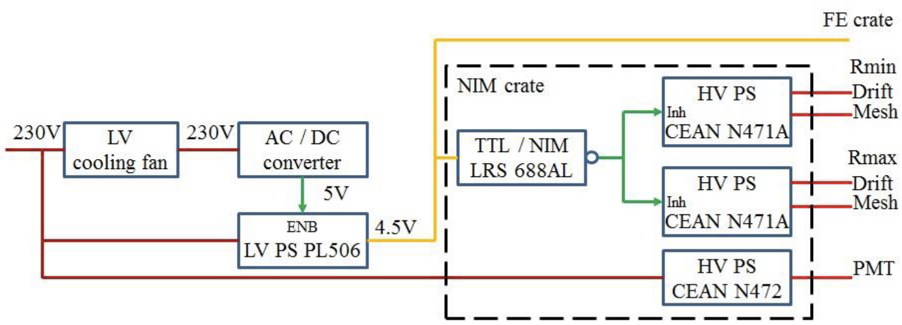

Figure 4.25: A block diagram of interlock system[22].

4.3 Frontend unit electronics

Analog signal from a strip is stored and digitized. A DREAM chip (described in subsection 5.1.2) can process 64 channels in parallel. 8 DREAMs are mounted on one frontend unit (described in subsection 5.1.1). Then we have prepared 4 fronted units to process 1432 strips at the same time.

4.3.1 Configuration of FEU board

The frontend unit (FEU) electronics for AMT has been developed in CEA Saclay[23]. A picture of FEU board is shown in Figure 4.26. The FEU board mainly consists of the DREAM chip, flash ADC, signal connector, optical protection and FPGA system. Analog signal from a strip is fed to one of the FEUs to be processed. In the FEU the signal fed to a DREAM through an optical protection to avoid the risk of damaging the DREAM electronics due to the sparks. The signal is amplified, shaped and stored on the DREAM. Processed signal is converted to the digital values on the 12-bit flash ADC. Neighbor 64 strips are grouped together and fed to a FEU with a micro-coaxial cable. 8 cables are connected to a FEU board.

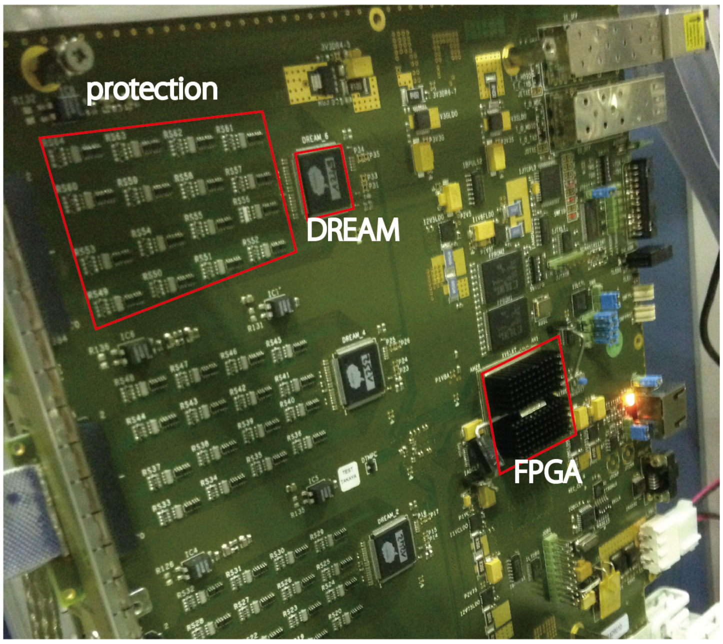

Figure 4.26: A picture of the FEU board for AMT.

4.3.2 DREAM chip

To analyze the signal from the detector, analog signals have to be amplified, shaped, discriminated and digitized. The AMT readout system has adopted special ASIC called DREAM chip which has been developed for Clas12 MicroMEGAS Vertex Tracker[24]. The DREAM stands for Dead-timeless Read-out Electron ASIC for MicroMEGAS, which can perform a dead-time less operation upto several tens of kilohertz trigger rate as its name suggests.

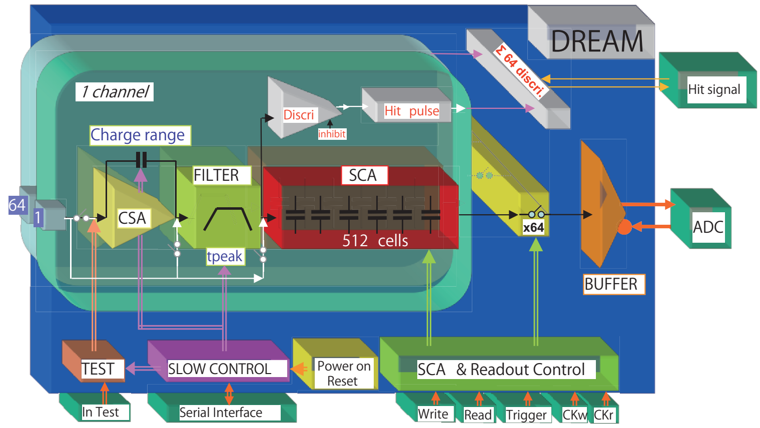

Figure 4.27: A schematic structure of the DREAM chip circuit[25].

Figure 4.27 shows a schematic structure of the DREAM chip circuit. A DREAM chip integrates 64 channels. Each channel can read each strip of the detector. The DREAM channel mainly consists of Charge Sensitive Amplifier(CSA), Shaper(FILTER), Switched Capacitor Array(SCA) and also Discriminator(Discri). An analog signal is first sent to the CSA to be amplified. The gain is programmable between 50 pC and 600 fC of a dynamic range. After amplification, signal goes to a FILTER to be shaped. The peaking time is selectable between 50 ns and 900 ns in sixteen values. The charge range of a CSA and the peaking time of the Shaper can be changed and selected by Slow control on the chip. This can be controlled with a serial interface. The output from the Shaper is fed to a SCA to be continuously sampled and stored on a 512-cell analog memory. The sampling frequency is also variable from 1 MHz to 50 MHz by the external control. The external control can select SCA cells marked by the external trigger to be read out. A 12-bit external ADC at a frequency up to 20 kHz is available to obtain the signal information. In parallel, the shaped signal is also fed to the Discriminator. The logical output from the Discriminator of all 64 channels are connected to the logical OR circuit to make internal trigger pulse.

Table 4.7 is a list of the main requirements for the DREAM chip. For the detector signals, DREAM input dynamic range is set to be 200 fC, peaking time value is set to be 180 ns and sampling frequency is set to 16.7 MHz. The external ADC is 12bit:4096 values. That is, 200 fC is corresponding to 4096 ADC bins. Therefore, 1 ADC bin is corresponding to 0.05 fC, which is, in principle, equivalent to the charge of 310 electrons. One of the DREAM chips is connected to the scintillator PMT. Scintillator signals are relatively higher than strip ones. Thus the input dynamic range of that DREAM chip is set to be 600 fC not to be saturated.

Parameter	Value
Number of channel	64
Input dynamic range	50, 100, 200, 600fC, selectable per channel
Peaking time value	50ns to 900ns (16 values)
Sampling Frequency	1MHz to 50MHz
Trigger rate	Up to 20kHz (4 samples read/trigger)
Counting rate	$<$ 50kHz/channel

Table 4.7: A list of the main requirements for DREAM chip[25].

4.3.3 Event sampling system

All strip signals are continuously pre-amplified, shaped, sampled at 20 MHz and kept in a circular analog memory as shown in Figure 4.28(a). Because of large-capacity data, in general the per-channel zero suppression is usually performed as shown in Figure 4.28(b), (c): at each trigger sampling starts with 16 μs latency. If the first several samples are above a programmable threshold, all 16 samples are retained, otherwise empty events are removed. Thus the capacity of the data can be compressed and a lot of data can be stored in a computer.

In addition, FEUs can implement additional two calculations: pedestal equalization, common mode noise correction. The explanation of these calculations is described below.

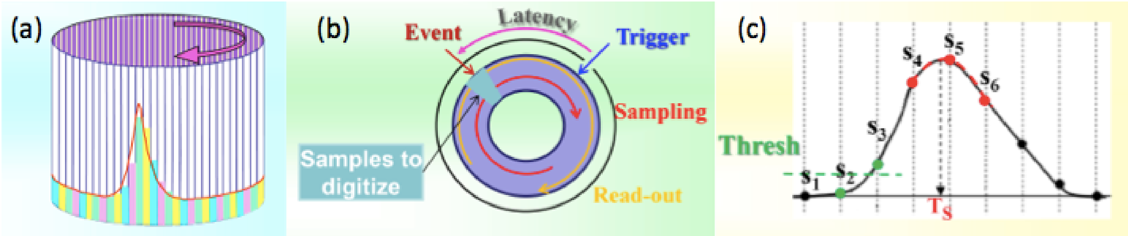

Figure 4.28: Illustrations of data sampling system.[22]. (a)An image of analog circular memory. (b)An image of sampling process. (c)An image of selected samples over threshold or not.

Pedestal equalization

Due to the PCB configuration, each strip has a different length. Thus each strip has a different electrical offset called pedestal. The pedestal offsets have to be removed for an accurate data analysis. After equalization and subtraction of these pedestals, offsets of all channels are equalized flatly around baseline. This pedestal equalization is done by a special pedestal run with a constant or random trigger. After taking 1000 events, 16000 pedestal measurements per channel are given because 16 samples are taken in each event per channel. From this run, pedestal averages are calculated for each channel to be subtracted from the event data.

Common mode noise correction

Regardless of any signals, the values are fluctuated due to the electrical noise. If the cause of this noise derives from electrical common mode noise, fluctuations can be reduced. In case of the common mode noise on the strips, if you pick up the medians of grouped 32 neighbor channels per each sample, deviations from the median at a certain sample are turned out to be roughly the same while ADC values of median of each sample are quite different. In order to apply the common mode noise correction, the median values of each sample have to be picked up and subtracted from the event data. Thus, after correction we can obtain relatively small random noise throughout all time samples.

4.4 Gas operation

4.4.1 Selected gas mixture

For the AMT detector, gas mixture of Ar and iC_4H_{10}(isobutane) were chosen while the various mixtures, such as He, Ne as a noble gas and CO_2 as a quencher gas, are used in other various experiments. As can be seen in Table 4.8 in Chapter 2, Ar has lower W-value (average energy expended ion pair formed) and higher energy loss than those of other noble gases. A lot of primary electrons are expected to be produced, which leads us to obtain large signal after amplification. Therefore Ar is often selected as noble gas for mixture. We chose iC_4H_{10} as quencher gas although high density iC_4H_{10} was designated to be flammable gas while CO_2 is non-flammable. To get high gain with the mixture of CO_2, much high electric field has to be applied in the amplification region. Due to sparks or discharge, which can occur easily, Bulk-MicroMEGAS would not work well. Therefore iC_4H_{10} was chosen, which make us possible to get high gain in lower electric field. However in recent days, so-called resistive MicroMEGAS was developed in CEA-Saclay, whose anode strips are coated with resistive films to avoid unwanted sparks on the strips. ATLAS in CERN has been used it for their requirements. Since expected signals in ATLAS experiment should be high flux rate, high electric field was required to count all signals without any dead time. This technique enabled to allow to energize much higher voltage between mesh and strips with using CO_2 as quencher gas.

Gas	Rate(%)	Use	Comment
Ar:iC_4H_{10}	95:5	The gain test	non-flammable gas
Ar:iC_4H_{10}	90:10	The experiment	flammable gas

Table 4.8: The list of gas mixture rate.

4.4.2 Gain of the MicroMEGAS

It is general to use a ^{55}Fe X-ray source for the gain determination of the gaseous detector. When the 5.9 keV X-ray from the source is injected into the MicroMEGAS, it ionizes the Ar atom by freeing a K-shell electron. Because the binding energy of the K-shell electron is 3.2 keV, the electron with a kinetic energy of 2.7 keV is released. In addition, when the excited Ar atom returns to the ground state with a transition of a electron from the peripheral shell to the vacant K-shell, an auger electron can be released with a probability of 85%. The auger electron have a kinetic energy of 3.2 keV which corresponds to the binding energy of the K-shell electron of Ar atom. Therefore total 5.9 keV electrons are released with a probability of 85%, which lose all of their energy in the Ar gas. On the other hand the rest of 15 % creates 3.2 keV characteristic X-ray. Because it doesn't interact with any electrons, the kinetic energy of the released electrons becomes 2.7 keV with a probability of 15 %.

Since the W value of Ar atom is 26 eV, the number of primary electrons can be calculated as

$$Number\ of\ primary\ electrons = \frac{5.9 \times 10^3 \text{ eV}}{26 \text{ eV}} \tag{4.6}$$

$$\sim 2.3 \times 10^2 \tag{4.7}$$

If we know the number of amplified electrons calculated from the detected charges, the gain of the MicroMEGAS is obtained as

$$gain = \frac{Number\ of\ amplified\ electrons}{Number\ of\ primary\ electrons}. \tag{4.8}$$

In the previous experiment, the gain of the AMT was measured as 1×10^4 with $\mathrm{Ar} : \mathrm{iC_4H_{10}} = 95 : 5$ gases, the drift voltage: -800V and the mesh voltage: -450V, although we have not measured the gain for the practical AMT condition (drift: -1600V, mesh: -470V with 10% $\mathrm{iC_4H_{10}}$). The gain information is listed on Table 4.9.

Parameter	Value
AMT gain	1×10^4
Mesh voltage	-400 V
Drift voltage	-800 V
Gas flowing	Regularly (1 atm)

Table 4.9: A list of parameters in the gain test of the AMT.

4.4.3 Gas flowing system

Figure 4.29 shows a diagram for the Gas flowing system of AMT. The gas flowing system consists of Switching, Pressure regulator, Flowmeter, Bubbler. The gas pressure from the bottle is tuned adequately by Manometers. At the Switching, Mixed gas is selected for the AMT experiment while Nitrogen gas is sometimes used for cleaning and purging the MicroMEGAS detector volume. The gas pressure is regulated again, and finally gas flow rate is tuned to around 5 liters per hour.
Regulated gas goes along the RED arrow in the Figure 4.29. After going through the layers, the gas goes into the liquid in the Bubbler OUT. When gas is flowing, bubbles are formed continuously in the liquid.
However, if somewhere inside layers gets clogged, the gas goes along the BLUE arrow to the Bubbler IN. To see some bubbles in the Bubbler IN, that is to say, there is a problem in the gas system.

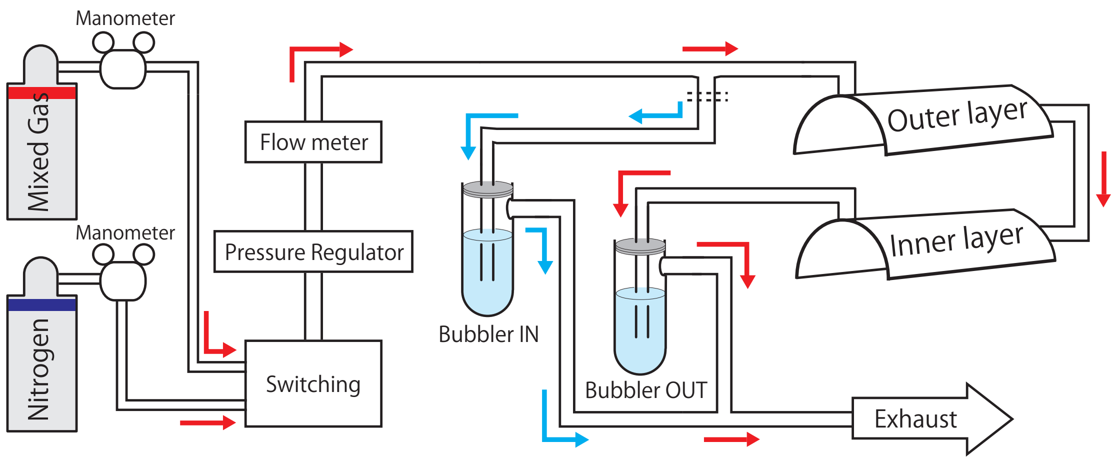

Figure 4.29: A diagram of the gas flowing system of AMT.

Figure 4.30 is a picture of gas flow and regulator panel mounted on the AMT rack. The mixed gas which contains Ar and iC_4H_{10} is flowing inside layers continuously to keep gas fresh. If the gas is not flowing, produced positively charged Ar ions are collected on the mesh and cathode. This cause the decrease of the electric field, which leads to a discharge or decrease of a signal detection efficiency of MicroMEGAS.

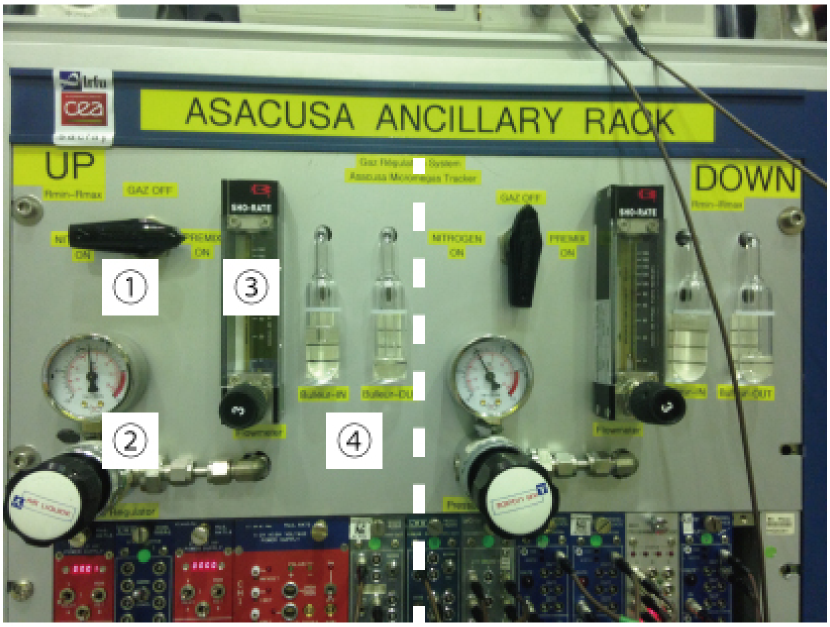

UP part	
1	Switching
2	Pressure Regulator
3	Flowmeter
4	Bubbler IN / OUT
DOWN part	
Not used	

Figure 4.30: A picture of gas flow and regulator panel mounted on the AMT rack.

Chapter 5

Vertex reconstruction process

In this chapter, a procedure of the vertex reconstruction is described in detail. In section 5.1, we explain how to obtain cluster information from strip signal, which is called “clusterization”. In section 5.2, a further discrimination applied for the antihydrogen experiment using CUSP trap is described. In section 5.3, a tracking method using Kalman-filter is described. In section 5.4, a vertex determination using POCA method is described. By using this algorithm, we finally obtained the 3-dimensional vertex positions. The results is described in chapter 6.

5.1 Clusterization

A charged particle which passes through the AMT generates an avalanche of secondary electrons in the amplification region, and deposits electric charge to several anode strips. These strips are grouped together and called a “cluster”. A cluster

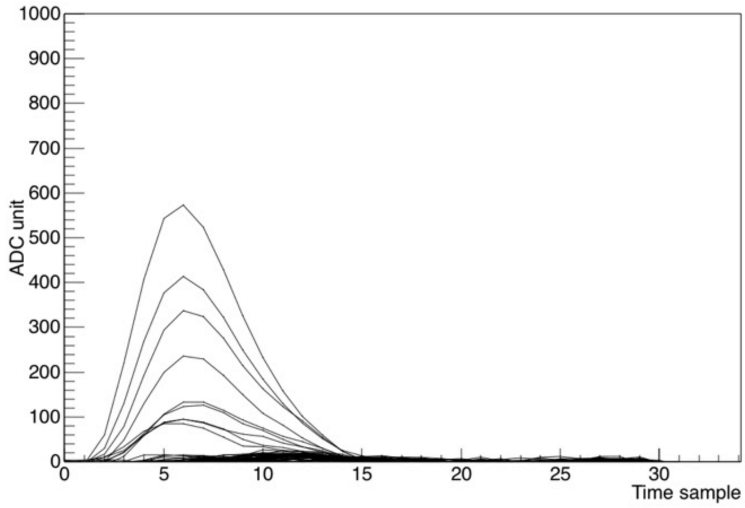

Figure 5.1: An example of strip signals of a cosmic ray event.(1 time sample: 48 ns, 1 ADC unit: 0.05 fC.

has various information such as how many strips belong to one cluster, what the total amount of charge is in one cluster, which strip has the maximum signal at what time and so forth. Since all this information has characteristic values of the event of a flying particle, it is useful to analyze them to estimate the position passed by a particle and to distinguish a signal from electric noise. Analysis to form clusters from signals on strips is called "clusterization".

Figure 5.1 shows an example of strip signals of a cosmic ray event. The pedestal and the common mode noise correction are subtracted. Each line in the figure represents individual strip signal in AMT. As explained in chapter 4, DREAM records the charges on the strips in digitized value consecutively with a fixed time interval. In this example, we recorded the signal for the period of 32 time samples in ADC unit (sampling frequency was 48 ns), but in the experiment we recorded for 16 time samples (sampling frequency was 60 ns). 1 ADC unit was 0.05 fC.

5.1.1 Definition of the specific values

Cluster size

In Figure 5.1, neighboring 64 strips are displayed on the same window so that we can see easily how many strips are active in one event. Figure 5.2 shows an image of cluster size. The number of the active strips in one cluster is called cluster size.

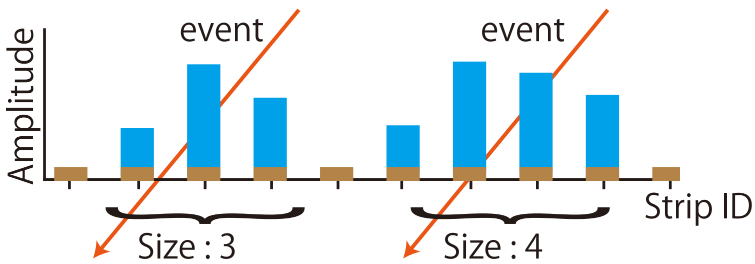

Figure 5.2: A schematic drawing of an image of the cluster size.

Figure 5.3 shows specific values during clusterization.

Strip max amplitude

From a comparison of each time sample of one strip in one cluster, the largest ADC value is found, which is called "Strip Max Amplitude". The range of the amplitude of particle event should be from 100 to more than 1000 ADC units on

12-bit DREAM chip with dynamic range of 200 fC, while in case of electric noise the amplitude should be much lower. Those low signals are due to the fluctuation of electric noise.

Max sample time

As seen in Figure 5.1, all time samples of cosmic event have reached maximum around 6 (in units of time samples) while in case of random noise its samples would have no peak pattern and independent of the time. A time which has the largest ADC values among recorded 16 samples is called "max sample time".

Max strip time

the extremum time calculated by quadratic function by fitting three samples around max sample is called "max strip time".

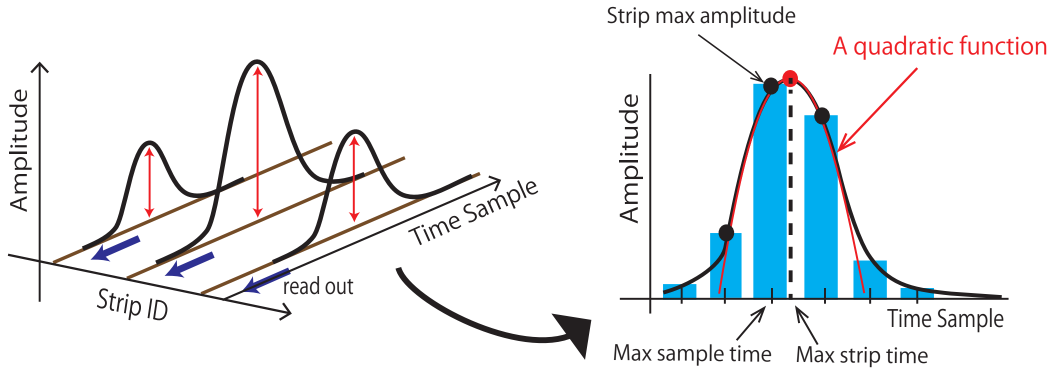

Figure 5.3: Image of strip amplitude, max sample time, max strip time.

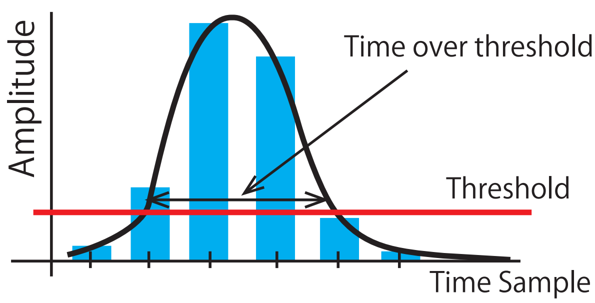

Figure 5.4: Image of time over threshold.

Time over threshold (TOT)

Figure 5.4 shows an image of time over threshold. We set a threshold level at a little bit above the baseline noise. A time over threshold is defined as a duration of signal above threshold. Signals which have a too long or short TOT might be noise to be ignored.

Cluster position

Figure 5.5 schematically shows the way to extract the cluster position which the particle had passed through. In the case where the cluster size is one, the position is where the hit strip is located. In the case where the cluster size is more than one, the position is obtained from the averaged position of strips in the cluster weighted by each strip's strip amplitude.

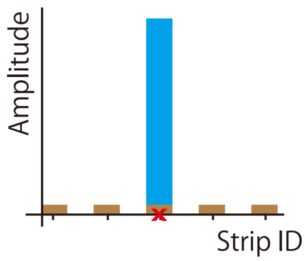

(a) Cluster Size: 1

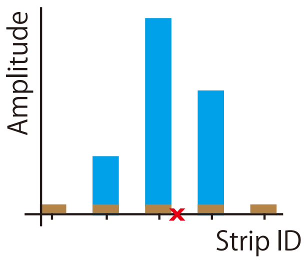

(b) Cluster Size: 3

Figure 5.5: A schematic drawing of an images of the clusters position in case of cluster size 1(a) and 3(b).

5.1.2 Cluster finding on each projection

Cluster position determination

1. When triggered, 16 time samples are sampled for each strip, and the pulse is recorded in ADC values.

2. The maximum pulse height among 16 samples is defined as Max Strip Amplitude(MaxStripAmpl). Due to the electric noise, strips are fluctuating around baseline values every time. Then RMS (root mean square) of the ADC values can be defined.

3. If MaxStripAmpl $\geq \sigma \times$ RMS, it is recognized as "signal", otherwise is ignored. The σ is the threshold level of the discriminator.

4. When signal is found on the strip, the neighboring strips are processed whether their signal is above the discriminator threshold.

5. Then the number of active strips is defined as "cluster size". For each strip in a cluster the strip ID and the sum of amplitudes are also recorded.

6. For each cluster, a weight averaged cluster position, X, is calculated as

$$X = \frac{iA_i + (i+1)A_{i+1} + (i+2)A_{i+2} + \cdots}{A_i + A_{i+1} + A_{i+2} + \cdots} = \frac{\sum_i iA_i}{\sum_i A_i} \tag{5.1}$$

   where i is the strip ID and A_i is the maximum pulse amplitude of strip i.

7. Then the position of the cluster is determined for each projection of C and Z strips.

Cluster merging

Figure 5.6 shows one of the possible signal distributions. Flying charged particle should make one cluster on each projection. But sometimes some strips in the cluster may not produce signal above threshold due to any strip problem, noise or inhomogeneous propagation of electrons. (a) shows that two clusters are produced from one charged particle. The clusters have to be merged as shown in (b). In the following steps, we can judge clusters if they have to be merged or not.

1. When we define i, j as the different cluster IDs, $X_{i,j}$ as the cluster position of cluster i, j and d as a certain distance, if $|X_i - X_j| < d$, we judge those clusters as one cluster. we typically define the d as 10 strips.

2. Then new merged cluster position is defined as averaged position of the original clusters.

3. After all, more realistic cluster distribution is obtained. Characteristic parameters of each merged cluster, such as cluster size, total amplitude and so on, are also redefined as the sum of original parameters of clusters.

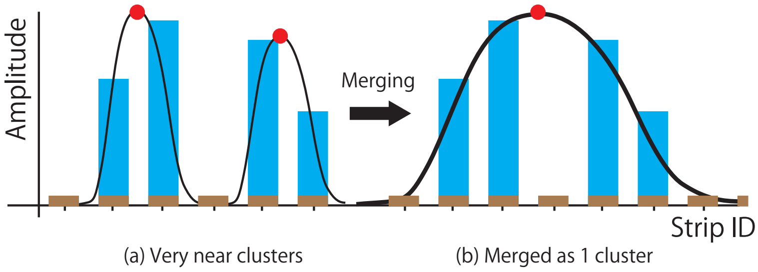

Figure 5.6: A schematic drawing of an image of merged cluster. (a) before merged. (b) after merged.

5.1.3 Clusters matching between inner and outer layer

In the following, we find a combination of a cluster on inner layer and a cluster on outer layer. Then we judge which combination is most likely. A true track should be going through almost the same region on both layers, so that we should have a cluster in each layer which has roughly the same coordinate.

Matching of Z clusters

We have 4 scintillator bars between two layers along Z direction. We know that the position of each scintillator bars and also strip numbers covered with each scintillator bars, as shown in Table 5.1. In order to match clusters between inner and outer layer, we take the following steps.

1. First a cluster finding algorithm is applied on the Z strip signals.
2. Then starting with the outer layer, the cluster position overlap with trigger scintillator area is determined.
3. The algorithm finds a cluster within the same region in inner layer. Then a possible combination is determined.
4. Such an algorithm can be applied to all clusters in the Z projection.

Matching of C clusters

In the next steps, we apply the following selection to the C clusters. Although there is no scintillators along the C strip, the principle is a similar way.

Scintillator bar label	Outer layer strip	Inner layer strip
NW	0-70	0-60
NNW	70-140	60-120
NNE	140-220	120-190
NE	220-290	190-250

Table 5.1: Trigger scintillators and corresponding inner and outer layer strips IDs.

1. In the case of a real track, the cluster position difference on two layers should be within 10 strips along C direction. So we set a typical value for the cut as 10 strips.
2. If there is a suitable cluster on both layers after Z and C selections, the 2D coordinates (C, Z) of each clusters are determined.
3. The possible cluster combination is called "hit pair". We can make tracks with hit pairs after 3D coordinate conversion and further selection described in the following subsection.

5.1.4 3D coordinate conversion of clusters position

In the following, we transform its coordinate from 2D detector strip coordinates (C, Z) into 3D position coordinates (x, y, z) as shown in Figure 5.7.

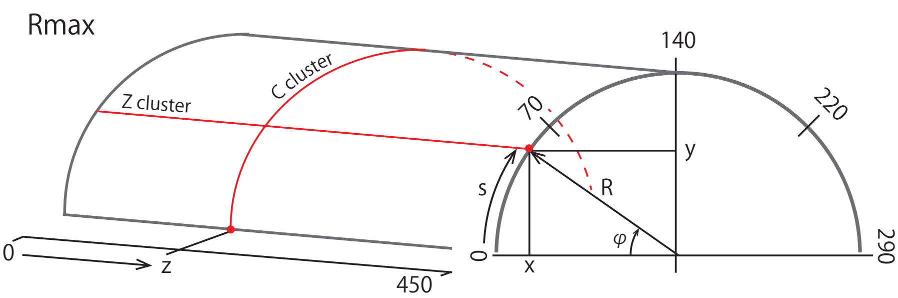

Figure 5.7: A schematic drawing of 3D conversion.

Now we have a cluster position along Z and C, which is expressed as the number of strips from the first strip(N_z, N_c). Furthermore the radius(R) of each layer and the pitch size of strip(d) are already defined geometrically. Therefore the arc length(s) can be calculated by

$$s = N_z d. \tag{5.2}$$

With the angle(φ) at the circumference, the arc length is also defined as

$$s = R\varphi \tag{5.3}$$

so that

$$\varphi = \frac{s}{R} = \frac{N_z d}{R}. \tag{5.4}$$

Therefore 3D position in Cartesian coordinates can be expressed as

$$x = R\cos\varphi = R\cos(N_z d/R) \tag{5.5}$$
$$y = R\sin\varphi = R\sin(N_z d/R) \tag{5.6}$$
$$z = N_c d. \tag{5.7}$$

5.2 Discrimination for the CUSP experiment

Figure 5.8 shows an illustration of two additional selections which is applicable to CUSP experiment. Among the possible cluster combinations, angular difference dφ between φ_1 and φ_2 hit coordinates is measured. In case of pion track coming from around the centre of axis position, the angular difference in the hit coordinates should be very small. In order to remove other fake tracks which have a large dφ, an additional selection like d$\varphi < \varphi_0$ is applied. The φ_0 can have a small value,

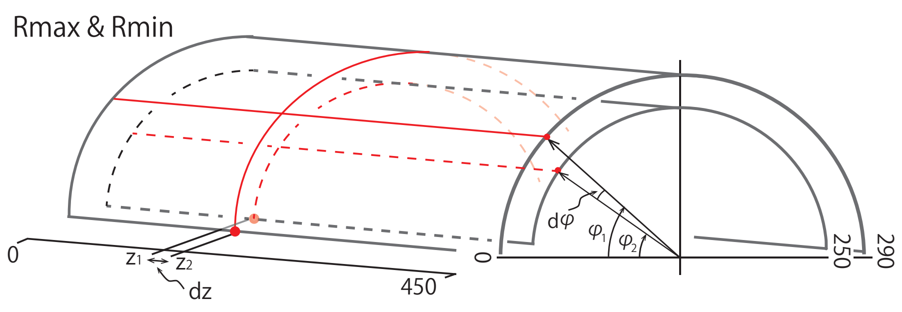

Figure 5.8: An illustration of dφ and dz.

depending on the data condition. Furthermore position difference dz along z-axis is also measured and d$z < z_0$ is applied as another additional selection. The z_0 can also have a small value which depends on the pion impact angle.

In this analysis the φ_0 discrimination is set to 0.05 radian which corresponds to 4 mm arc length. In case of pions released from antiproton annihilation at the centre of axis of the cylinder, d$s = 4$ mm is a very loose value. It is expected that the cluster position difference of the real pion track between two layers along C strip shouldn't be farther than the order of mm.

Furthermore the z_0 discrimination is set to be 10 mm in distance which corresponds to 45$\circ$ impact angle of traks. Tracks whose impact angle is more than 45° should be improbable.

Thus the candidates of the possible hit pairs are well optimized for the CUSP experiment and finally we can make tracks with these hit pairs.

5.3 Tracking method

Once hit pairs are selected, tracks can be fitted with a Kalman-filter method[26, 27]. Using the Kalman-filter, a particle state including spacial vectors, momentum vectors, charge and mass of the particle, is initialized on the outer layer of the detector, and an initial direction of a track in three dimension is assumed. Here we assume a spatial vector which points from the hit position in the outer layer to that in the inner layer. Then the particle state is evolved from the outer layer until the particle reaches the inner layer by solving the equations of motion in three dimension. At this point the calculated particle position can be compared with the measured inner layer hit position, and a correction can be applied using the Kalman-filter equations. The procedure can be repeated backwards, that is, from the inner layer to the outer layer for some number of time, until the required position determination is fulfilled.

5.4 Vertex determination using POCA

Figure 5.9 shows a vertex reconstruction from two tracks. After the fitting procedure of a track with Kalman-filter method is finished, recorded events with at least 2 tracks are further processed. All the tracks are propagated through the whole detector in three dimensions. For each pair of tracks, the point of closest approach (POCA) and the closest approach distance (d_{POCA}) of the pair is determined. Good two track combination should have a small POCA distance. In this analysis a discrimination of POCA distance is set as $d_{POCA} < 1$ cm. This means that only when the POCA distance is smaller than 1 cm, the POCA is accepted as a realistic vertex of tracks.

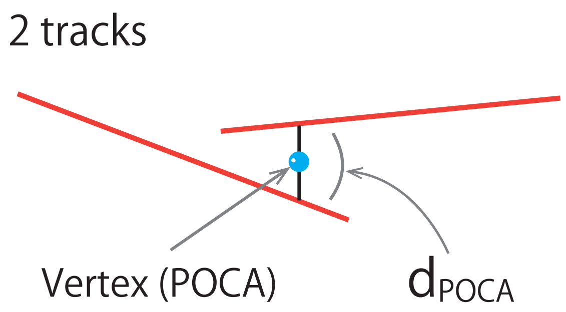

Figure 5.9: An illustration of an image of the POCA method. The red lines are the tracks. The blue dot is the POCAs. The distance, d_{POCA}, between two tracks and POCA are defined.

5.5 Configuration of the processed data

Processed data is sent to the data acquisition PC and stored. The format of the data is fdf (Feu Data File), which is a raw binary file containing full pulse information. For the following analysis, the data is converted into the following two files based on ROOT[28].

FirstCycle

The goal of FirstCycle is to reduce the size of data by extracting parametrized pulse height, pulse width, pulse time, time-over-threshold, strip ID information for each channel. During the process the pedestal subtraction, common mode noise correction, zero-suppression and channel masking on demand are applied to the data.

SecondCycle

The reduced data from FirstCycle is processed further in a SecondCycle, where cluster finding algorithm (details provided in the previous sections), trigger logic, hit pairing, tracking and vertex finding is applied on the data. Finally, histograms are produced from the obtained variables.

Chapter 6

Experimental results

In this Chapter, the experimental results of AMT are shown and discussed. In section 6.1, results taken in the cosmic ray measurement are described. In section 6.2, results taken in the antiproton trap measurement are described. In section 6.3, a result of a calibration measurement is described.

6.1 Cosmic ray measurement

We performed a cosmic ray measurement for the two purposes: checking the behavior of the AMT using cosmic ray; determination of discrimination level to reduce electric noises. Because the AMT was installed into CUSP trap for the first time, it was necessary to check the correct behavior of the AMT before the beamtime on 2014. Also we had to check the behavior of electric noises on the strips which could disturb the vertex reconstruction.

During the measurements the candidates of charged particles coming to the AMT were expected to be (a)muons in the cosmic ray, (b)electrons/positrons in the cosmic ray and (c)electrons produced by a multiple scattering of a cosmic particle. However since the AMT has been thickly covered with a solenoid magnet and its magnetic shield, the rate of muons coming to the AMT might be lower than expected. On the other hand the rate of the multiple scattering should be increased due to the heavy-metal apparatus covering the AMT.

6.1.1 Condition of the measurement

Table 6.1 shows the experimental condition of the cosmic ray measurement. The measurement was continued for 24 hours to accumulate the data sufficiently. This is because the rate of the cosmic ray was not so high. During the measurements, the magnetic field had been switched off. The mixed gases had been flowing regularly. The mesh and the drift voltages of each layer were -450 V and -800 V, respectively.

Parameter	Values
Measurement duration time	24 hours
Magnetic field	OFF
Gas flowing	Regularly (1 atm)
Mesh voltage of each layer	-450 V
Drift voltage of each layer	-800 V

Table 6.1: A list of the condition of the cosmic ray measurement.

6.1.2 Clusters distribution

Figure 6.1 and Figure 6.2 show cluster position distributions on the inner layer(Rmin) and the outer layer(Rmax), respectively. We have two projections on each layer. C projection has 448 curved strips along circumference. Z projection has 248(Rmin), 288(Rmax) straight strips which are lined along Z direction(described in 4.3 in detail).

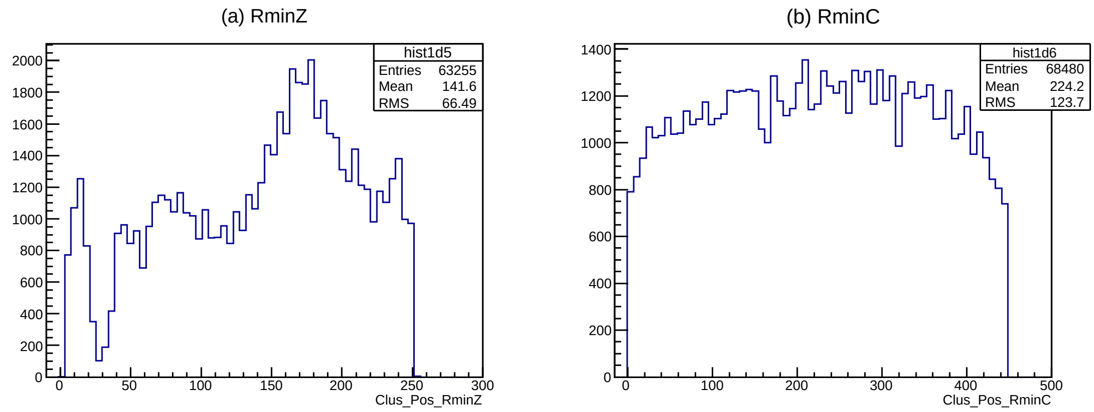

Figure 6.1: Cluster position distributions on (a)RminZ and (b)RminC in the cosmic ray measurement.

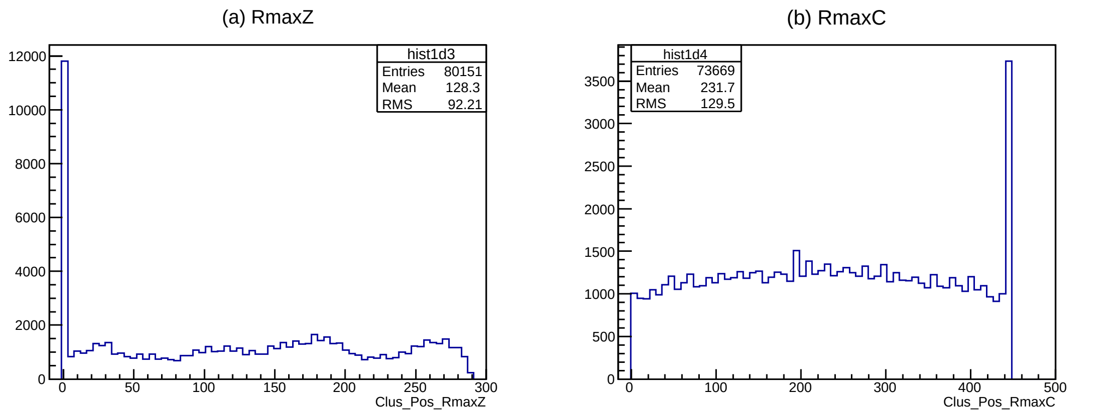

Figure 6.2: Cluster position distributions on (a)RmaxZ and (b)RmaxC in the cosmic ray measurement.

The RminZ cosmic ray distribution shows a reduced number of clusters around strip ID 20-40, which is due to electrical noise problems in these channels. This does not put any principle problem in the case of antiproton annihilation vertex distribution, it only means that these electric channels are present as "bad channels" or "dead area". On the other hand RminC has a flat distribution. This is due to a symmetric layout of the C strips.

On Rmax layer, the both projections have a hot channel on the edge of the layer. Due to the mechanical connection the edge seems to be affected by the electric noise. They should be a fake cluster which have to be removed for the following analysis.

6.1.3 Determination of discrimination level

Signal pulse height maximum time and time over threshold

Figure 6.3(a) shows a 2D histogram between signal pulse height maximum time and time over threshold (TOT) on RmaxZ taken by the cosmic ray measurement. When charged particles produce detectable signals in the AMT the signal pulse height maximum time and time over threshold has a characteristic value, while the electric noise produces rather random pulses with random pulse height maximum time and time over threshold values. As seen in the Figure, most of the clusters were likely to have the cluster pulse height maximum time around 5 and the cluster TOT between 2-12. Otherwise clusters which have too short or too long cluster pulse height maximum time and TOT should be made by the electric noises. Those should be removed. Therefore we finally determined the discrimination level as $3 < \text{time} < 7$, $2 < \text{TOT} < 12$. With these discriminations the events within a

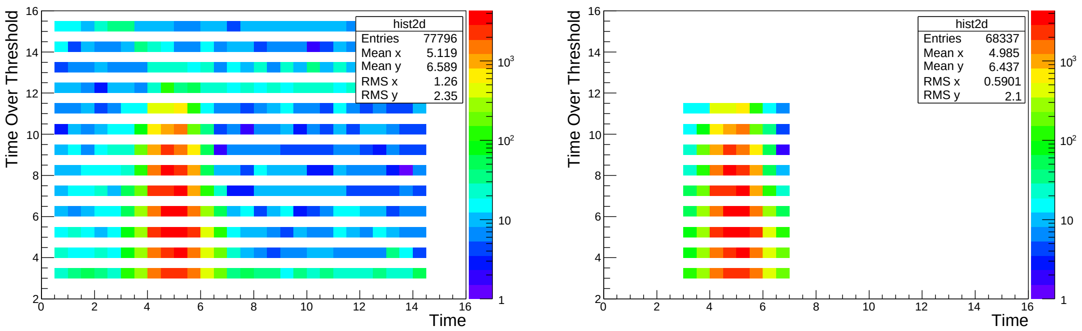

(a) (b)

Figure 6.3: 2D histograms of signal pulse height maximum time and TOT (a)before selection and (b)after selection.

square shown in Figure 6.3(b) were remained.

With the determined discrimination the hot channel on Rmax shown in Figure 6.2 was reduced significantly. Obtained the new cluster position distributions of Rmax layer are shown in Figure 6.4. As can be seen in the RmaxZ distribution, there are four bumps at the same interval of the strips region. They are due to the noise pattern in the detector strips, and the 4-fold structure reflects the four FEU cables used to read out the Z strips.

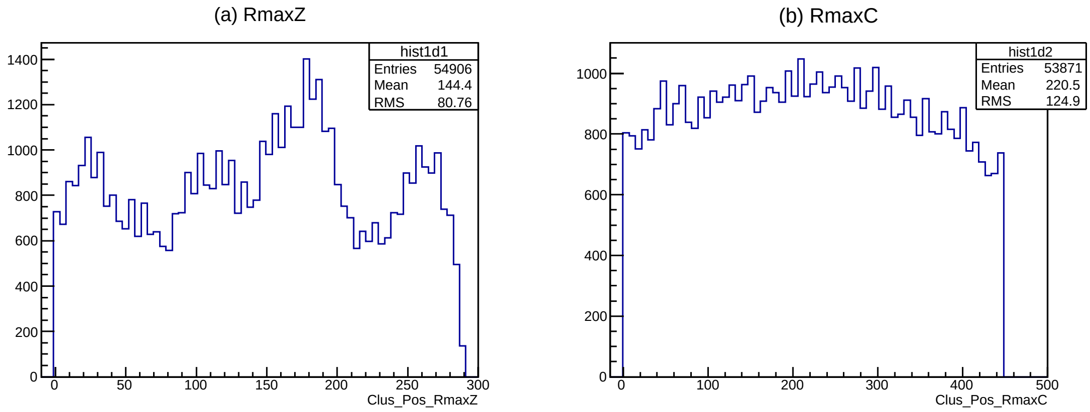

Figure 6.4: cosmic ray cluster position distribution on (a)RmaxZ and (b)RmaxC.

6.1.4 2D mapping of clusters position distribution

Figure 6.5 shows a 2D mapping of cluster position distribution on (a)Rmax layer and (b)Rmin layer. In every triggered event we have clusters on both C and Z projections. Then the cluster detector strip coordinate (C, Z) is determined and plotted on a two-dimensional map. We can see both efficient regions and inefficient regions, which are due to some low-efficient strips.

When a charged particle goes through the AMT, a scintillator bar gets active and Rmax and Rmin should have a cluster at the same time. The active strips should be located on the area covered by the active scintillator bar. Therefore it is important for a demonstration of the AMT performance to check the triggered events which have clusters on an expected region of both layers. Figure 6.6 shows a 2D position mapping when NNE scintillator bar is triggering. In both layers obviously the area overlapped with NNE bar is active and counts more than other areas. This indicates that the most triggered events are expected to be real charged particle events rather than fake events caused by noises..

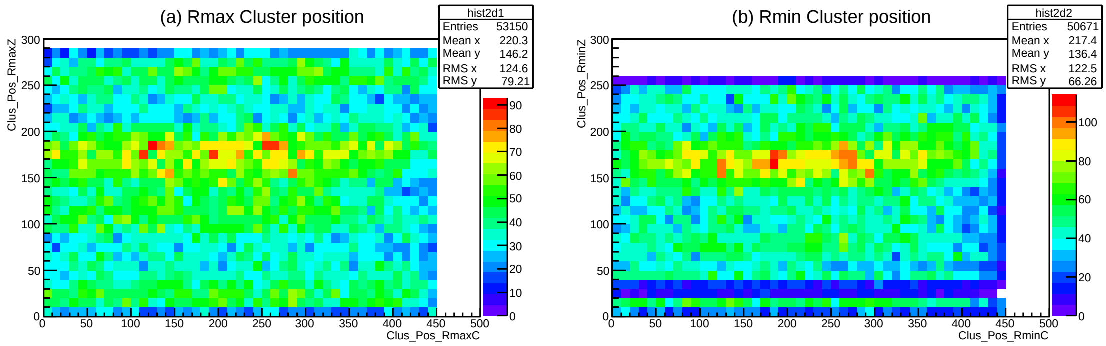

Figure 6.5: 2D mappings of cluster position distributions on (a)Rmax layer and (b)Rmin layer.

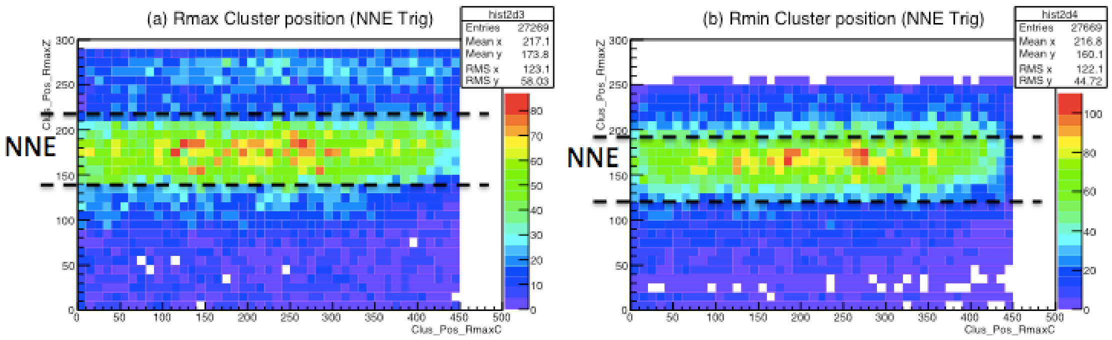

Figure 6.6: 2D mappings of cluster position distributions after selection on (a)Rmax layer and (b)Rmin layer. The black lines are the rough boundaries of NNE scintillator bar.

6.2 Antiproton annihilation measurement

6.2.1 Condition of the measurement

We have trapped antiproton plasma at 3 different positions in the trap without any positrons. During the measurements antiprotons were trapped at (a)U5, (b)U7 (c)U9 electrode for 600 s. During trap measurement, the AMT detector was recording pion tracks hit signals from annihilation events. In the following sections the data will be discussed with figures.

Antiprotons were injected into the CUSP trap with 150 eV kinetic energy, and were captured and cooled for the first 30 s. Then they were trapped in an electrostatic harmonic potential with electrons. The cooled antiproton cloud behaves as a non-neutral plasma. The shape of the antiproton cloud was expected to be a spheroid. Because there were no positrons trapped in the trap, antiprotons were able to be annihilated with only residual gases at around the center-axis where they were trapped. After the confinement for 600 s, antiprotons were extracted to the upstream side. Various parameters of the measurement condition are summarized in Table 6.2.

Parameter	Values
Injection energy of $\bar{\mathrm{p}}$s	150 eV
Cooling time	30 s
Confinement time	600 s
Extraction time	10 s
Estimated number of e^{-}s	3×10^{7}
Trapped positions	U5, U7, U9
Magnitude of magnetic field at the center of harmonic potential	1.5T, 2T, 1.5T
Gas flowing	Regularly (1 atm)
Mesh voltage of each layer	-470 V
Drift voltage of each layer	-1600 V

Table 6.2: A list of the condition of the antiproton trap measurement.

6.2.2 Event rate

Figure 6.7 shows the event rate of the AMT detector for the U7 trap measurement U7. The bin size was set to be 1 s. Thus the number of events per 1 s can be extracted from the figure. Here the event is defined as triggered count of the AMT with 2-fold or more coincidence.

As seen in this histogram, the event rate increased suddenly as high as several kHz and decreased suddenly as background level after a few minutes. This reaction of AMT was obviously synchronized with the phase of the antiproton trap measurement. This means that the event rate increased just after the injection of antiprotons into the CUSP. Then the event rate decreased gradually while antiprotons were trapped because the antiprotons were constantly collided with the residual gases and annihilated. This resulted in decreasing the number of trapped antiprotons. Furthermore there was a sharp peak at the end. The reason can be explained as the signal of antiproton annihilations when extracted antiprotons were diverged and annihilated all together on the wall of the MRE. We can conclude that our AMT was able to detect pions caused by the antiproton annihilations around several kHz and the event rate decreased over time as expected and consistent with other detectors.

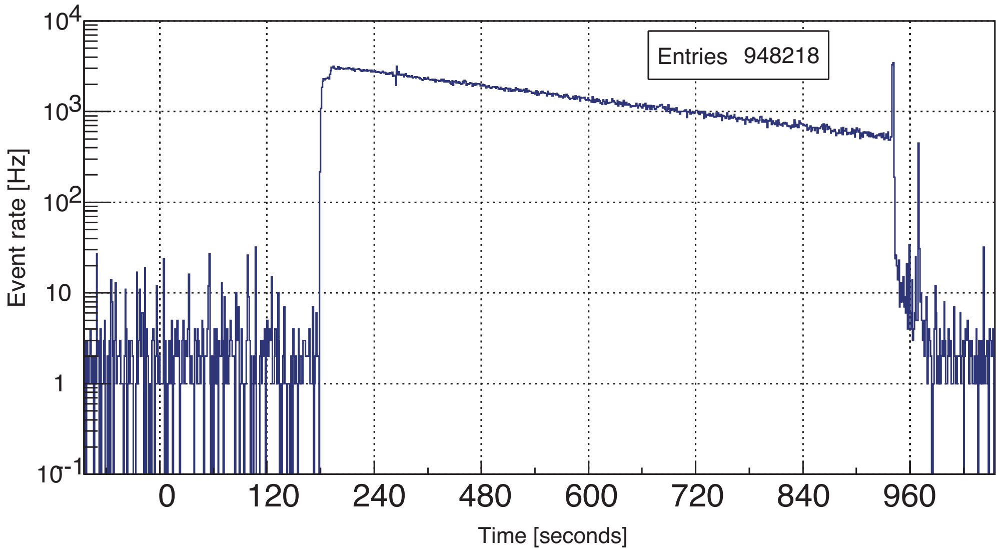

Figure 6.7: A distribution of the event rate during the annihilation of $\bar{\text{p}}$s for 600 s.

6.2.3 Scintillators multiplicity

Figure 6.8 shows the difference of signals of one of the PMT between (a)the cosmic-ray measurement and (b)the antiproton annihilation measurement. The AMT has eight scintillator bars to provide a trigger. A trigger signal was generated by any scintillator signal above the preset threshold. In both measurements the event which had a 2-fold coincidence or more was triggered. When there was a trigger, all eight PMT signals are recorded. A scintillator had a signal around baseline of the ADC values when there was an event triggered by the other scintillators. Thus in Figure 6.8(a) there was a peak below 600 ADC which was the baseline ADC value of the non-active PMTs. Just above 1000 ADC, there was another peak. The peak was only visible in case of very low-rate cosmic ray detection, it was not present during high-rate antiproton annihilation detection, which suggested that it was created by some effect related to very low-rate signals. Then we set a software threshold at 900 ADC (Red line) for the trigger condition of the cosmic-ray measurement.

In the antiproton measurements the PMT signal distribution was shown in Figure 6.8(b). From the result of the cosmic ray measurement, we set the preset threshold to be 600 ADC (Red line) to remove the baseline values.

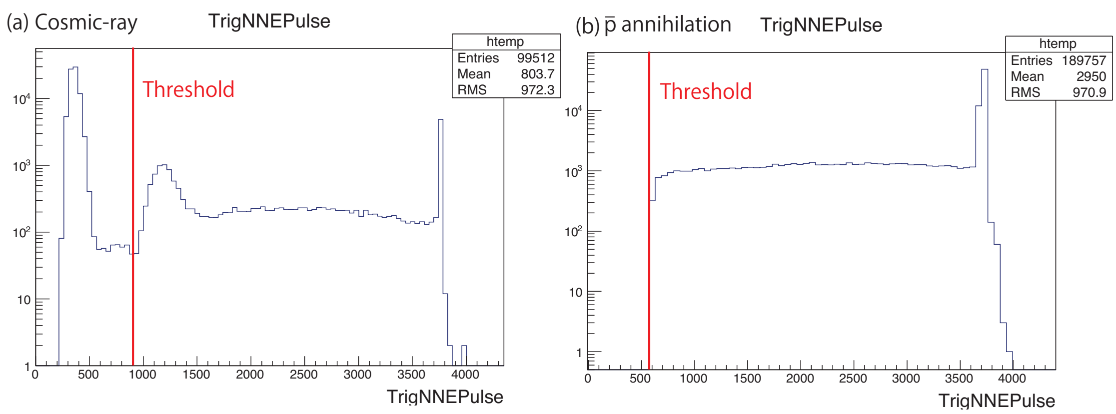

Figure 6.8: Distributions of NNE scintillator's PMT signal during (a)cosmic ray and (b)antiproton trap measurement.

Figure 6.9 shows the difference of the multiplicity of the AMT scintillators between (a)the cosmic-ray measurement and (b)the antiproton annihilation measurement. The multiplicity means the number of active scintillators for one event. Muons in the cosmic-ray passing through the AMT make two scintillators active in principle. In fact as shown in Figure 6.9(a), the most probable multiplicity seems to be two.

This indicates that the AMT detected signals of cosmic ray correctly.

The number of released pions has been expected to be around 2-4[29]. From the antiproton measurement, the most probable observed multiplicities was 3 or 4, as can be seen in Figure 6.9(b).

From these results of cosmic and antiproton measurement, our scintillator bars clearly observed the annihilation reaction in CUSP trap.

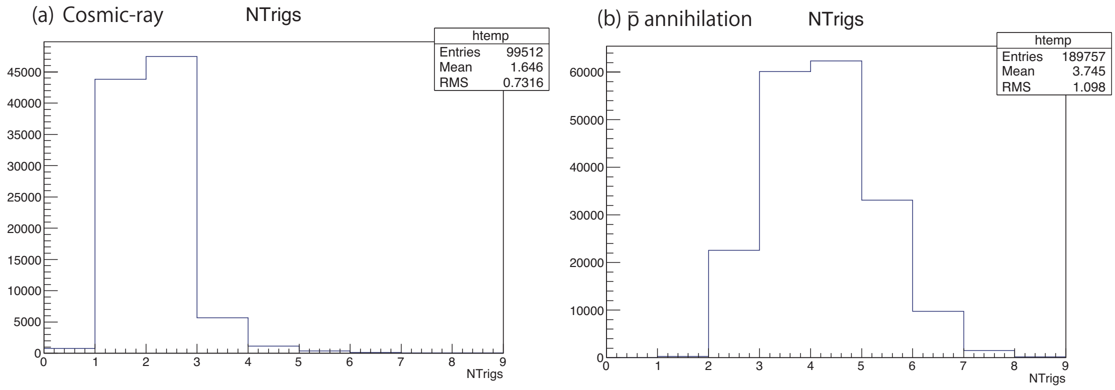

Figure 6.9: Scintillator multiplicity distributions of cosmic ray and antiproton trap measurement.

6.2.4 Distribution of clusters

Figure 6.10 shows cluster size distributions in the 4 readout projections. As seen in this figure, most clusters seem to have cluster size of 1: electric charges are induced on only one strip. This can be explained by the expectation (from simulations with Garfield++[30]) that a typical size of electron avalanche in the amplification region is smaller than the strip width. In addition, there is a clear difference of cluster size tendencies between C and Z projection. From a comparison of C and Z distribution, the cluster size of C projection contains relatively larger components than that of Z projection. It is expected that pions released from antiproton annihilations have large impact angle against C strips because in the antiproton trap experiment the annihilation due to the collision between antiproton and residual gases occurred at around the axis and pions are released isotopically from there. Therefore it is a natural result that the cluster size of C projection is larger than that of Z projection.

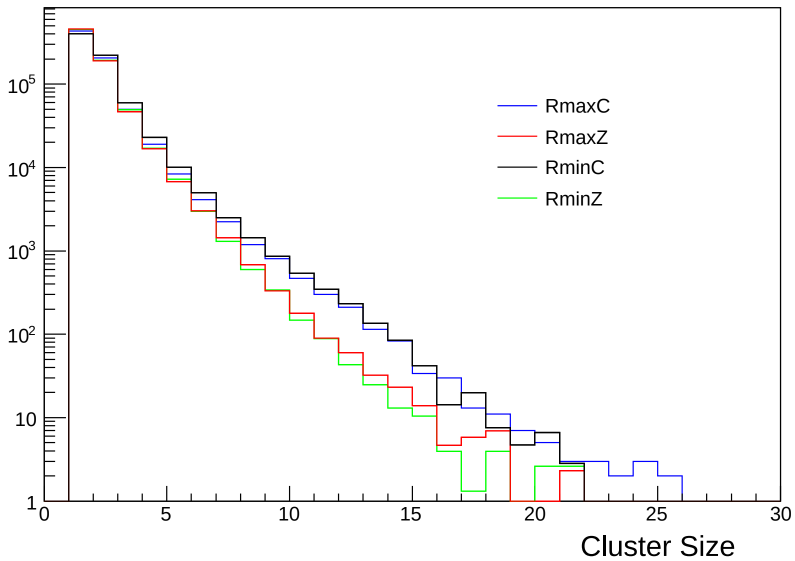

Figure 6.10: Cluster size distributions of 4 projections.

Figure 6.11(a) shows distributions of strip maximum pulse height amplitude in all clusters of the 4 projections. They are expressed as ADC unit. From a comparison of the 4 projections, there is not so much difference among them. Most signals are around several hundreds in ADC unit. Due to the limitation of dynamic range around 4000 ADC, there is a peak at the end because of the saturation. It can be assumed that there was no deficiency on any projections, that is, the 4 projections were all in the same efficiency.

Figure 6.11(b) is a distribution of Max strip time of all strips in all clusters. All the 4 projections had roughly the same distribution. This result indicates that the DAQ system performed in good synchrony with the trigger and timing. Also electric noise was negligible.

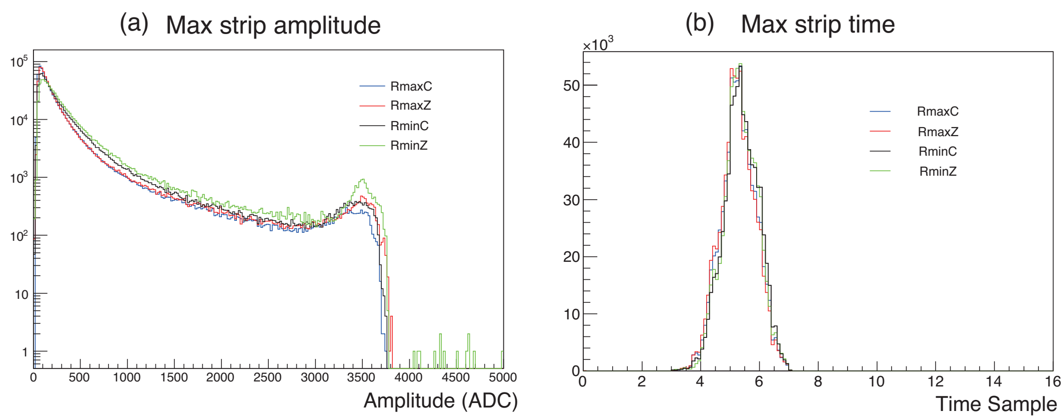

Figure 6.11: Distributions of (a)Max Strip Amplitude and (b)Max Strip Time.

6.2.5 Clusters matching between inner and outer layer

When we suppose a cluster on Rmax, there should be a cluster on Rmin as well due to the small distance between outer layer (Rmax) and inner layer (Rmin). The coordinate of the cluster is expected to be similar as that on Rmax. An actual detected cluster distribution is shown in Figure 6.12. The created clusters positions (strip coordinates of each projection) on both layers are expressed as 2D histogram of Rmax as x-axis and Rmin as y-axis. As seen in C projection of Figure 6.12(a), there are many clusters making a diagonal line of 2D histogram. This indicates that two clusters on both layers in one event have roughly the same coordinates on C projections. Also as seen in Z projection of Figure 6.12(b), there is, of course, a similar distribution although the number of strips of RmaxZ and RminZ covering a region is different. It is concluded that the most of clusters created by the same particle have similar coordinates.

A track produced by connecting those coordinates can be a candidate of a realistic track of a particle. On the other hand a pair of clusters with a long distance should make unrealistic track because those pairs are not likely to be real particle tracks. From the two distributions, most of the events seem to have an ideal cluster condition to successfully fit a particle track.

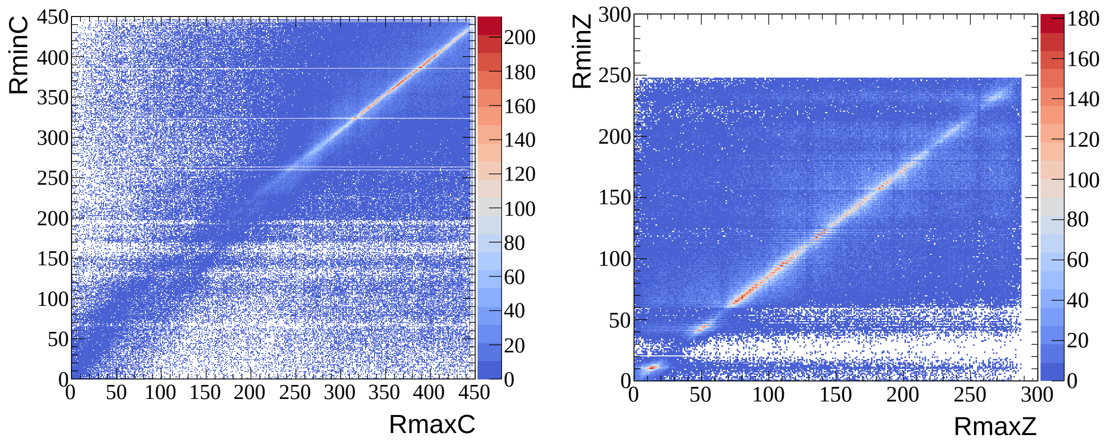

(a) RmaxC and RminC

(b) RmaxZ and RminZ

Figure 6.12: 2D mappings of cluster position difference of (a)RmaxC and RminC, (b)RmaxZ and RminZ.

6.2.6 Tracking of the clusters

After finding cluster pairs, we made tracks by fitting a line using Kalman-filter. Because actual tracks of charged pions were curved due to the magnetic field, we had to apply the Kalman-filter algorithm to hit pairs as a curved line fitting. However at the moment we had been under development of the algorithm which included the effect of the magnetic field. Then by assuming that the effect of the magnetic field should be low because most tracks of pions are expected to have large momenta, we used the algorithm to fit tracks with a straight track model.

Figure 6.13(a) shows a histogram of the number of tracks in each event. The number of pions released from antiproton annihilation was expected to be 2-4. But there were, nevertheless, 0 or 1 track events as can be seen in the figure. Those were due to missing a cluster on any projection. Because we were not able to fit tracks if a cluster was missed, those events resulted in 0 or 1 tracks. From the figure we found that the rate of those events were 80%. The 20% have at lease two tracks and should have at least 1 POCA. During the analysis of annihilation data, track and vertex findings were only executed in case there were at least 2 clusters in each projection; this method was employed in order to make the analysis faster. Figure 6.13(b) shows a histogram of the number of POCAs in each event. As described above, the 80% of all events resulted in 0 POCAs. When we define n as the number of tracks, the number of POCAs is calculated as ${}_nC_2$. Thus in the figure, events having 1, 3, 6 POCAs can be seen, otherwise events having 2, 4, 5 can not be seen.

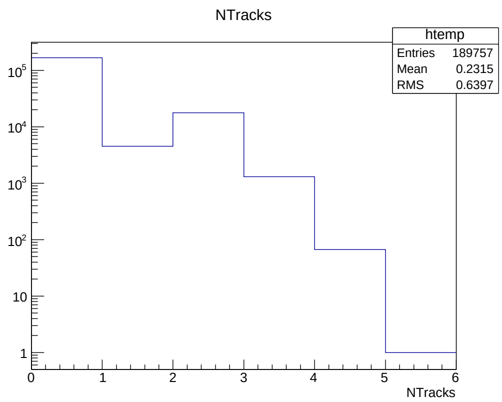

(a) Number of tracks.

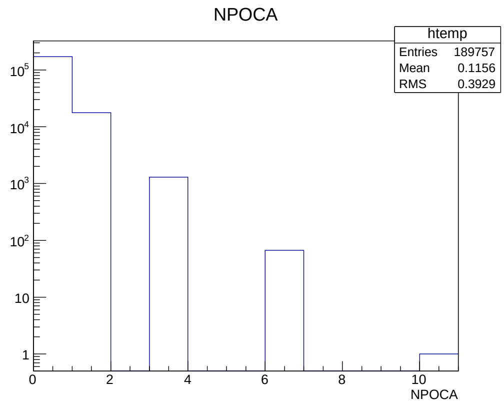

(b) Number of POCAs.

Figure 6.13: Histograms of (a)the number of tracks and (b)the number of POCAs.

Figure 6.14 is two examples which illustrate: (a)some good 2 hit-pairs make realistic POCAs at the center; (b)on the other hand, some of hit-pairs still make unlikely POCAs although they were correctly processed by the algorithm which contain various selections. The coordinates of the colored dots in the figure are some of the actual data taken in the experiment. From tens of thousands of correctly-processed events, a 3D histogram which contain all obtained POCAs are created, as shown in the following section.

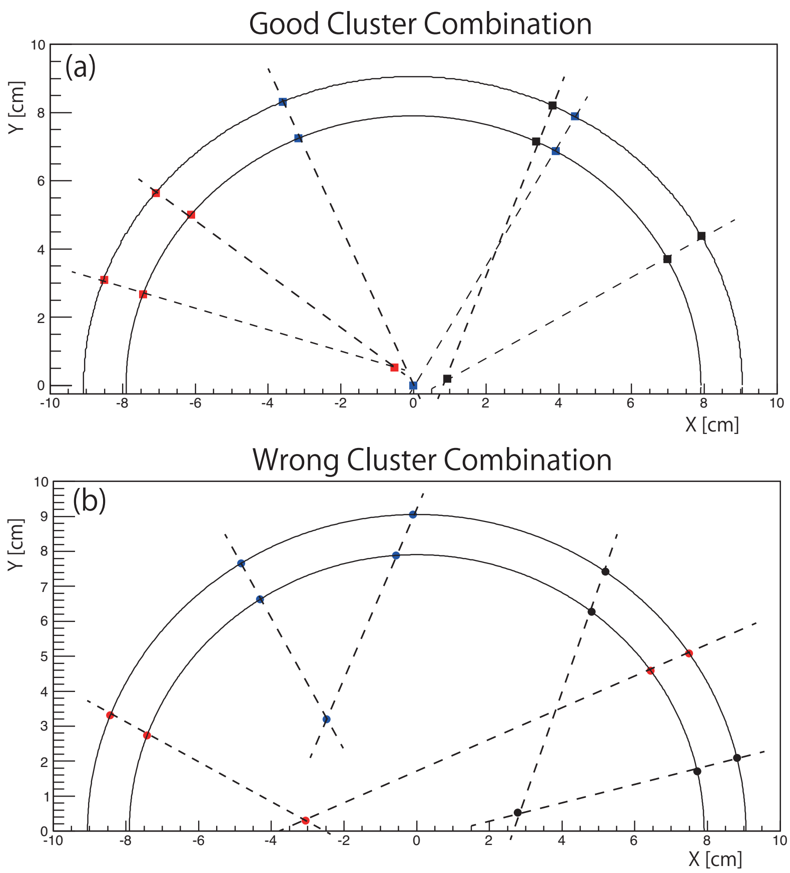

Figure 6.14: A drawing of hit pairs tracking which makes (a)good POCAs, (b)unlikely POCAs. The coordinates of colored dots in the figure are actual values.

6.2.7 3D mapping of reconstructed vertex distribution

As shown in Figure 6.15, we finally obtained a 3-dimensional mapping of reconstructed vertex distribution for the U7 trap measurement by using our current algorithm. From the distribution we also have 2-dimensionally-converted mappings shown in Figure 6.16 (a)the XY mapping, (b)the YZ mapping and (c)the XZ mapping. The discrimination of the POCA distance, $d_{POCA} < 1.0$ cm, has been applied to the current algorithm. The MicroMEGAS Rmax and Rmin layers have been also drawn in the XY mapping.

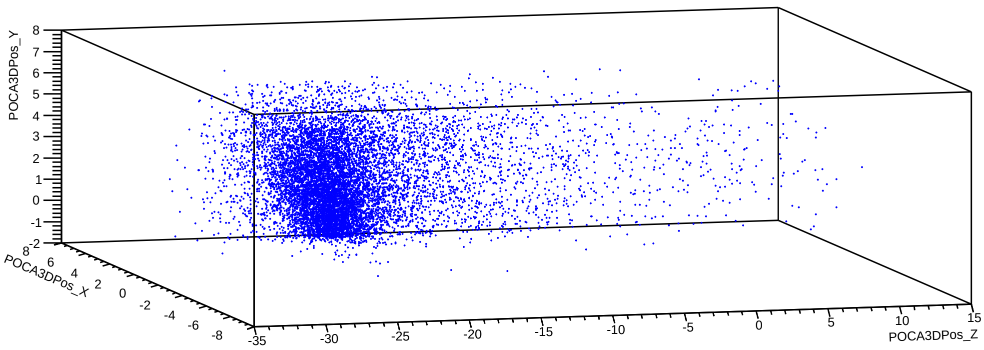

Figure 6.15: A 3D vertex distribution for U7 trap measurement. The unit is cm.

As seen in the XY distribution, obviously we can see a lot of obtained vertexes at the center. In order to estimate the reconstruction accuracy of the AMT, the XY distribution was converted into R distribution shown in Figure 6.17. Its full width at half maximum (FWHM) can be calculated at 1 cm. This result means that the AMT system can detect and reconstruct the antiproton annihilation with residual gases successfully. Also we can say that the accuracy is enough to distinguish annihilation of antihydrogen on MRE at r=4 cm from the annihilation of antiproton with residual gases on the center axis.

On the other hand, we can also see a halo in the XY distribution. Because the actual radius of the antiproton cloud was expected to be around 3 mm, the pions as annihilation products should not be released at a distance from the center. Therefore the large halo is due to some wrong combinations of tracks.

Furthermore the wrong combinations make unlikely vertexes on a Z distribution.

In addition, an expansion of the axial size of the antiproton cloud should be considered on the Z distribution rather than on XY distribution. Because there are a lot of reasons why there are so many unlikely vertexes, we will discuss some possible the reasons in the following.

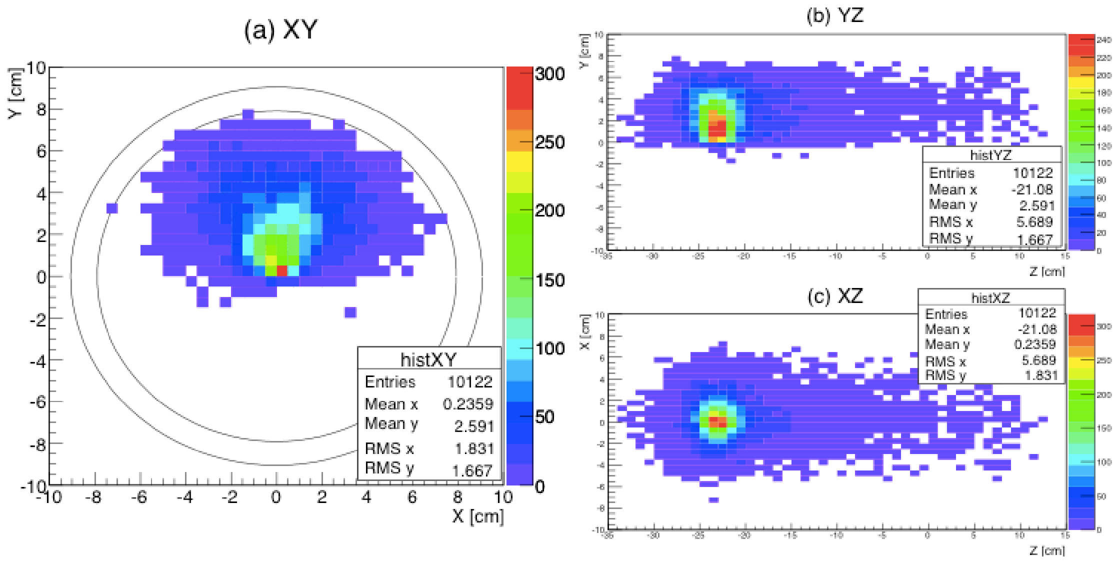

Figure 6.16: The vertex 2D distributions for U7 trap measurement. (a)the XY mapping, (b)the YZ mapping and (c)the XZ mapping.

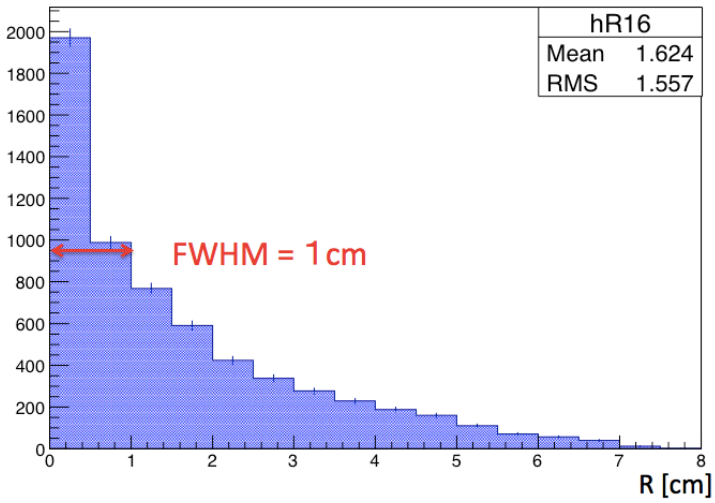

Figure 6.17: A vertex distribution shown as a faction of radius.

An effect of the scattering of pions

A thick stainless chamber and a MRE have been located on a passage of a pion. Some of pions should be scattered and change their momentum vectors. Those pions make some tracks whose direction is different from an initial direction. When the POCA method is applied to those tracks, obtained vertexes should appear on unlikely positions. This effect have to be considered for both R and Z distributions.

An effect of wrong combination of secondary electrons with primary pions

During the interaction of pions scattered in matter, some secondary electrons can be produced. Those electrons can interact with gases in MicroMEGAS as well and the signals are read out. When a track made by secondary electron and a track of primary pion are combined, a fake vertex appeared on unlikely position will be obtained. This effect have to be considered for both R and Z distributions.

An effect of the magnetic field.

Due to the strong magnetic field along Z-axis, a charged particle moves in a circular motion. Thus a passage of a released charged pion should be curved. Since we have not included the effect of the magnetic field in the track fitting algorithm yet, we can not obtain so precise vertex position. Moreover the eccentricity of the curvature depends on the pion's momentum. That is, a slow pion is highly affected by the magnetic field and make a highly-curved passage. The vertex should appear on unlikely position. This effect have to be considered for only R distribution.

An effect of trapped antiproton cloud expansion.

The antiprotons are uniformly distributed in the electrons cloud whose shape has been expected to be a spheroid. Its radial size and axial size depend on the number of electrons, the potential depth, and the magnetic field where the cloud is trapped. According to a reference[31], the potential distribution of plasma in electrostatic field is expressed as

$$\phi_T(r, z) = \phi_h(r, z) + \phi_s(r, z), \tag{6.1}$$

where $\phi_h(r, z)$ is the external hyperbolic potential, $\phi_s(r, z)$ is the self-field potential of the plasma, r and z are the length from the center of plasma to the boundary. Furthermore in case of the spheroidal plasma, we can obtain the relation among V_0 :potential difference, N_e :number of electrons, a :minor radius of spheroid, $\alpha = a/b$:aspect ratio, from the equation of

$$V_0 = \phi_T(R, L) - \phi_T(R, 0) \tag{6.2}$$

$$= \quad K\left[\alpha\left\{I\Big(\frac{R}{a},\frac{L}{a}\Big)-I\Big(\frac{R}{a},0\Big)\right\}-2(1-\gamma)\Big(\frac{L}{a}\Big)^2\right], \tag{6.3}$$

where K is a function of a, α and N_e. γ is a function of α. $I(\rho,\zeta)$ is a function of $\rho = r/a$, $\zeta = z/a$ and α. This relation indicates that if three of them, e.g.(V_0, N_e, a) are known, the remaining one(α) can be determined. From the α value, the axial length of the plasma, b, can be calculated.

From the previous experiment the radius of antiproton cloud, a, and the number of electrons, N_e, have been estimated to be around 3 mm (at U7) and 3×10^7 , respectively. Moreover we define the potential difference between the center and the edge of harmonic potential, V_0, as 50 V. Therefore the axial length of the electron plasma, b, at U7 has been calculated to be 1.3 cm. Thus the antiproton cloud is expected to be spread over around $2b \sim 3$ cm along z-axis. Therefore a vertex distribution obtained from the spheroidal cloud should become blurred.

Short summary

Since the radial size of trapped antiproton plasma is relatively small, a large halo in the XY distribution is obviously not due to the effect of the actual size of the cloud. The size of the plasma mainly affected the Z distribution. However the axial 3 cm cloud should definitely not release any pions at a distance from where the cloud trapped. Nevertheless as seen in Figure 6.16(b),(c), obtained vertexes seemed to be located there. They are also not due to the cloud effect but the other effects like scattered pions or secondary electrons.

When we discuss the resolution of AMT, we have to take into account those effects separately on XY resolution and Z resolution. So far it is difficult to estimate which effect is dominant on the resolution. But we can only say that the cloud effect is smaller than the other effects, such as the wrong combinations of secondary electrons and the curved tracks due to a magnetic field as discussed above.

6.3 Calibration of Z-axis

Antiproton trap measurements at U5, U7, U9 were performed. For each measurement, a harmonic potential well was prepared by the MRE. Antiprotons were trapped in this well. The electric potential distributions of the MRE are shown in Figure 6.18. Z-axis histograms of vertex distributions obtained from the 3 measurements are shown in Figure 6.19. The histograms have a peak which should correspond to the center of each electrode. The center of the peak was determined from gaussian fitting around a top of the peak. From the results, a position relation between the AMT and the MRE can be calibrated.

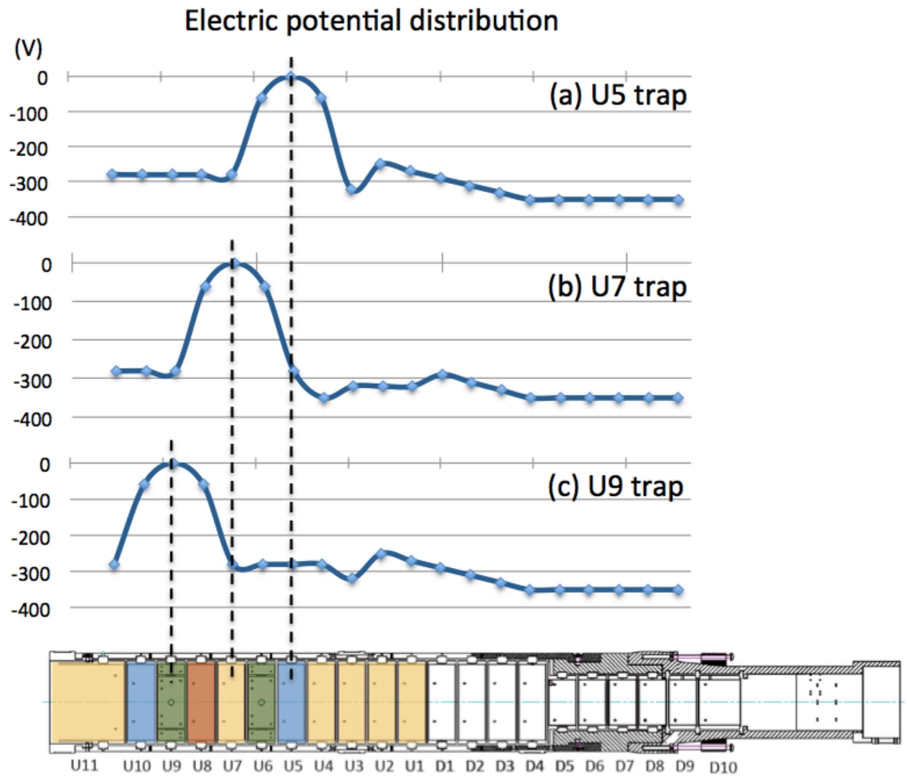

Figure 6.18: Electric potential distributions for (a)U5, (b)U7, (c)U9 trap measurements.

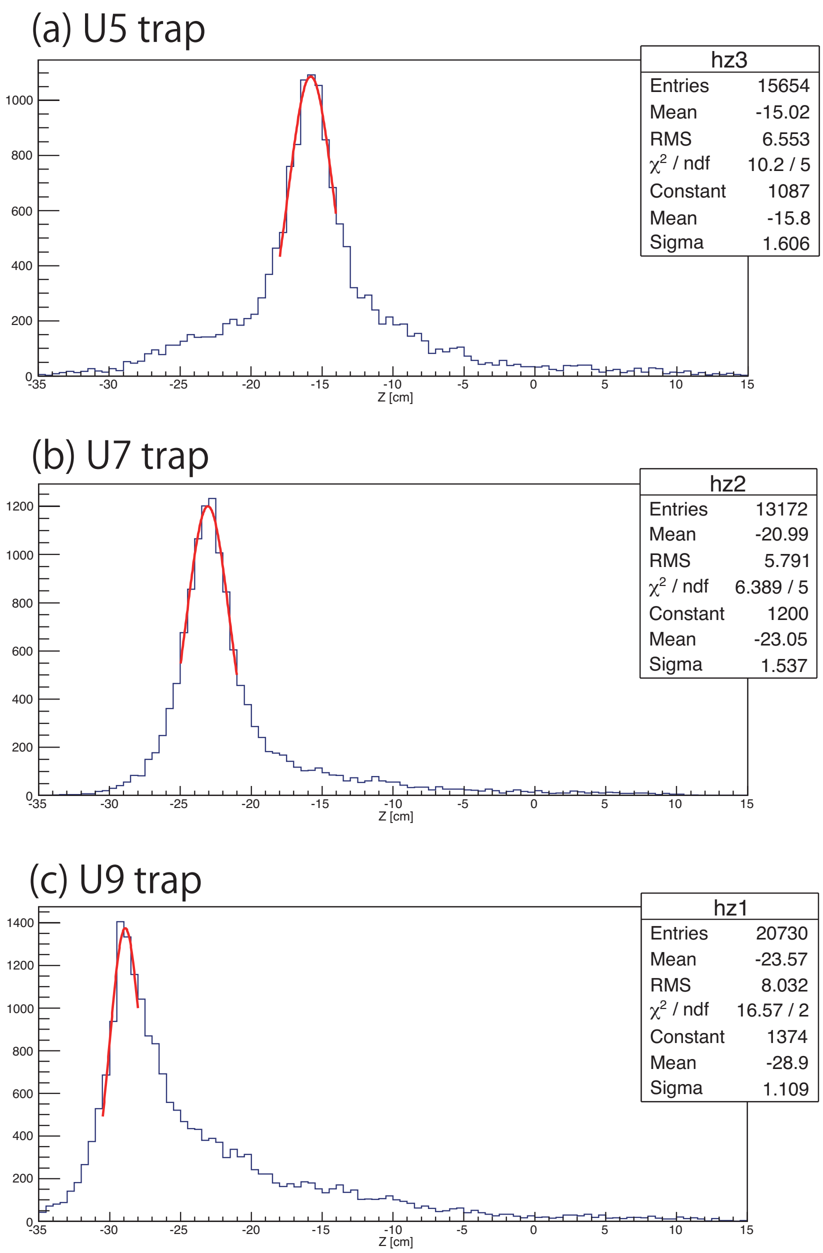

Figure 6.19: Histograms along Z-axis of (a)U5, (b)U7, (c)U9 trap measurements.

As seen in Figure 6.19(a), there is a symmetric distribution. However in Figure 6.19(b), (c), there are distributions which seem to have asymmetric tails. They are due to the difference of detector's solid angle of upstream side and downstream side for each annihilation.

As seen in Figure 6.20, the AMT covered the electrodes from U10 to U4 for 40 cm. The upstream side solid angle for antiproton annihilations gets smaller with approaching upstream edge. Thus near the edge, a reconstruction efficiency at the upstream side is lower than that at the downstream side. The electrode of U5 is located near the center, while the electrodes of U7 and U9 were located in a distance from center. Therefore the histograms obtained from U7 and U9 measurements have such a long asymmetric tails.

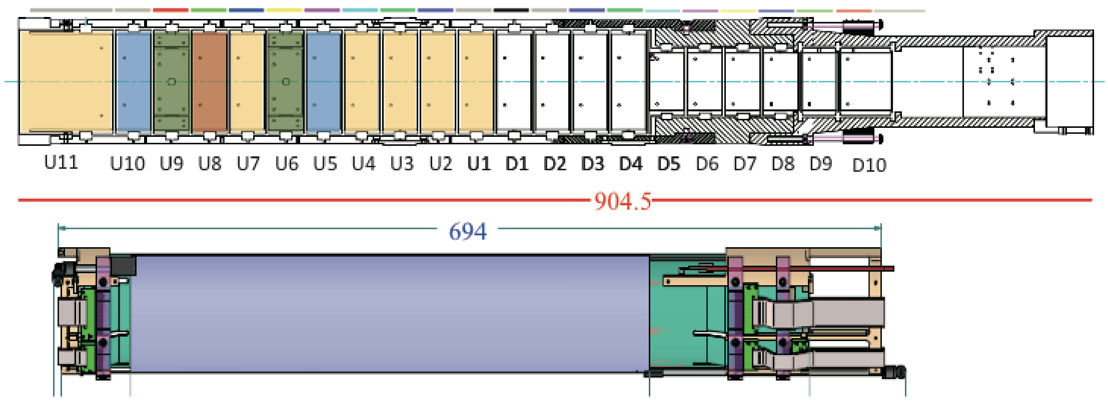

Figure 6.20: Position configuration between AMT and MRE.

Chapter 7

Conclusion

We have developed the ASACUSA MicroMEGAS Tracker (AMT) for 3D position determination of antihydrogen annihilation in the CUSP trap. In 2014, the AMT was successfully installed in the double cusp magnet. The AMT system consisted of two layers of half-cylindrical MicroMEGAS, a triggering system, a DAQ system and an algorithm for the reconstruction of vertices.

In the cosmic-ray measurement, we determined a discrimination level for a reduction of electric noises and checked the cluster distribution with the discrimination. When we selected the events which have a coincidence with a triggered scintillator bar, the events which produced clusters only within the region of the layer covered with the scintillator bar. The results indicated that we definitely confirmed the passage of charged particles, which means that the AMT has worked correctly.

From a result of the antiproton trap measurement for 600 s, we succeeded in detecting pions signals and reconstructed 1×10^4 vertices by using our current algorithm. Also we confirmed that 65% of the vertices within a circle of $r = 1$ cm centered at the z-axis where the antiprotons were expected to be localized. This result indicates that the AMT system can reconstruct true vertex positions with a high accuracy. Therefore by using the AMT, we should distinguish two kinds of antiproton annihilations: at the center with residual gases; on the wall of MRE resulting from antihydrogen formations.

However the algorithm in use has been under development and has not been included effects of the magnetic field yet. Also the various selections in the current algorithm have to be more optimized for the antihydrogen experiment. After finalizing the algorithm, we expect to reduce the combinatorial background in the vertex distribution and therefore improve the resolution of the annihilation vertex detection.

The AMT will become an important device for monitoring the antihydrogen formations three dimensionally.

Bibliography

[1] H. Hellwig et al. Measurement of the unperturbed hydrogen hyperfine transition frequency. *IEEE Transactions on Instrumentation and Measurement*, IM-19(4):200, 1970.

[2] L. Essen, R. W. Donaldson, M.J. Bangham, and E. G. Hope. Frequency of the hydrogen maser. *Nature*, 229(5280):110, 1971.

[3] L. S. Brown and G. Gabrielse. Geonium theory: Physics of a single electron or ion in a penning trap. *Rev. Mod. Phys.*, 58:223, 1986.

[4] J. E. Nafe and E. B. Nelson. The hyperfine structure of hydrogen and deuterium. *Physical Review*, 73(7):718, 1948.

[5] Y. Enomoto. *Antihydrogen production in cusp trap*. PhD thesis, University of Tokyo, 2010.

[6] Y. Enomoto et al. Synthesis of cold antihydrogen in a cusp trap. *Physical Review Letters*, 105(24):243401, 2010.

[7] private communication (paper being submitted).

[8] N. Kuroda et al. Antihydrogen atom formation in a cusp trap towards spin polarized beams. *Hyperfine Interact*, 212:31–40, 2012.

[9] William R. Leo. *Techniques for Nuclear and Particle Physics Experiments*. Springer, 1994.

[10] K.A. Olive et al. (Particle Data Group). 2014 review of particle physics. *Chin. Phys. C*, 38(090001), 2014.

[11] K. Nakamura et al.(PDG). 2010 review of particle physics. *Chin. Phys. C*, 37(075021), 2010.

[12] C. Amsler et al.(PDG). 2008 review of particle physics. *Physics Letters*, B667(1), 2008.

[13] Y. Giomataris. Micromegas: a high-granularity position-sensitive gaseous detector for high particle-flux environments. *Nuclear Instruments and Methods in Physics Research Section A*, 376, 1996.

[14] I. Giomataris. *MicroMEGAS: results and prospects.* CEA/Saclay, DAPNIA,91191 Gif-sur-Yvette Cedex. France.

[15] Hitachi. *Probe Cables.* http://www.hitachi-cable.com/products/cable/medical/medical/probe/index.html.

[16] Samtec. *75 Ohm 38, AWG Micro Coax Cable, Data sheet.* http://www.samtec.com/documents/webfiles/technical_library/TCF-3875F-XX-XX_datasheet.pdf.

[17] TOSHIBA. *Double Cusp Superconducting Magnet Instruction Manual.*

[18] Hamamatsu. *PHOTOMULTIPLIER TUBES -Basic and Application-.*

[19] R. Granelli. *Technical Design Report External Trigger System.* CEA Saclay.

[20] Saint Gobain. *BC408, Data sheet.* http://www.crystals.saint-gobain.com/uploadedFiles/SG-Crystals/Documents/SGC%20BC400-404-408-412-416%20Data%20Sheet.pdf.

[21] Saint Gobain. *BCF-91A, Data sheet.* http://www.crystals.saint-gobain.com/uploadedFiles/SG-Crystals/Documents/SGC%20Fibers%20Brochure.pdf.

[22] M. Combet, R. Granelli, Ph. Legou, and I. Mandjavidze. *The AMT installation.* CEA saclay, 8 2014.

[23] Irakli MANDJAVIDZE. *FEU a frontend unit for Micromegas trackers User' s Manual.* CEA Saclay, 9 2013.

[24] S. Anue et al. Micromegas tracker project for clas12. *Nuclear Instruments and Methods in Physics Research Section A*, 604, 2009.

[25] P. Baron, E. Delagnes, C.Flouzat, and F. Guilloux. *DREAM, a Front End ASIC for CLAS12 detector User Manual.* CLAS12, 1 2014.

[26] R.E. Kalman and R.S. Bucy. New results in linear filtering and prediction theory. *ASME*, J. Bas. Eng. 83D, 1961.

[27] R. Fruhwirth. Application of kalman filtering to track and vertex fitting. *Nucl. Instr. and Meth.*, A262, 1987.

[28] CERN. http://root.cern.ch.

[29] M. Hori et al. Analogcherenko v detectors used in laser spectroscopy experiments on antiprotonic helium. *Nuclear Instruments and Methods in Physics Research*, A 496, 2003.

[30] H. Schindler and Rob Veenhof. *Garfield++*. http://cern.ch/garfieldpp.

[31] Akihiro Mohri et al. Confinement of nonneutral spheroidal plasmas in multi-ring electrode traps. *Jpn. J. Appl. Phys.*, 37, 1998.

謝辞

初めに、担当教官として２年間ご指導して下さいました松田恭幸准教授に心から感謝いたします。松田先生は、私が修士 1 年の頃から夏の学校や学会、CERN への出張などを積極的に推奨して下さいました。私が修論を書くにあたり CERN での研究テーマを選んだのも、修士 1 年での経験があったからです。　山崎泰規特任教授は、修士の研究として AMT 開発という非常に興味深いテーマを与えて下さいました。今年度は初の AMT 実践導入ということもあり、最も重要でなタイミングで参加させて下さったことに深く感謝いたします。　鳥居寛之助教には学期中の放射線の講義で何度もお世話になりました。毎回興味深いお話が聞けるので、学部生用の授業にまで何度かお邪魔していました。　黒田直史助教には研究生活を通して様々な課題を頂きました。回路製作や機械設計などの知識を身につけるきっかけを下さったことに深く御礼申し上げます。また、CERN 滞在中のアドバイスは非常に役に立つ事ばかりで、不便無く生活できたのは黒田先生のお陰です。

CERN での活動では金井保之博士、檜垣浩之准教授、永田祐吾博士に大変お世話になりました。右も左も分かっていなかった私に施設内の注意点や実験装置の説明などを丁寧にしてくださいました。榎本嘉範博士は製作していた電気回路について非常に的確なご指摘を下さいました。榎本さん無くしては期限内に完成していなかったと思うと、感謝の念でいっぱいです。

研究室の先輩方である、田中香津生さん、大塚未来さん、高木聡さん、長濱弘季さん、水谷丈洋さん、田島美典さんは常に私を支えてくれる優しい方々でした。皆さん博識で、いつも興味深い話で長い時間話し込んでしまいました。　唯一の同期である樋口嵩くんとはこの２年間ほとんど一緒に行動してました。特に CERN 滞在中のシェアアパートでの生活は、一緒に食事を作ったりお互い忙しいのに夜遅くまで話し込んでしまったり、日々楽しく生活出来たのも樋口くんのお陰です。とっても感謝しています、ありがとう。

後輩の東芳隆くん、上野恭裕くん、田中陶冶くん、田邉大樹くんには力仕事やデータ解析などを手伝ってもらいました。研究室で下らない話なんかにも付き合わせてしまいました。CERN での旅行も楽しかったです。

海外渡航手続きや理研一般公開の際には理化学研究所山崎原子物理研究室秘書、和田ひとみさん、井澤真知子さん、森田めぐみさんにお世話になりました。丁寧なご説明と迅速なお手配にとても感謝しております。

最後に、大学院生活を通して私を支えてくれた家族、友人、その他すべての方々に厚く御礼申し上げます。

Acknowledgement

I would like to express my sincere gratitude to Dr. B. Radics for his continuous support of my master course. Without his encouraging tasks and helpful comments, the thesis would never been completed. I could not have imagined having a better advisor for my thesis and work on site.
I really appreciate Dr. D. J. Murtagh and Dr. S. V. Gorp spending a lot of time talking with me. Dan told me his cooking skill, Simon told me a growth of his son. Their talks had relaxed me.
In my daily work in the office Mr. M. Bartel gave me a kind help. His cheerful character had made a comradely atmosphere in the office.
I would like to thank to all the members of ASACUSA making welcoming atmosphere for me.
My sincere thanks also goes to CEA-Saclay collaborators. During the installation of the AMT, they had taught a lot of things in detail despite their crowded schedule. I really appreciate them.